The Astrophysical Journal, 653:739–755, 2006 December 10
© 2006. The American Astronomical Society. All rights reserved. Printed in U.S.A.

NUMERICAL MODELING OF MAGNETOHYDRODYNAMIC WAVE PROPAGATION AND REFRACTION IN SUNSPOTS

E. Khomenko[1,2] and M. Collados[1]
Received 2006 April 3; accepted 2006 July 14

ABSTRACT

We present numerical simulations of magnetoacoustic wave propagation from the photosphere to the low chromosphere in a magnetic sunspot-like structure. A thick flux tube, with dimensions typical of a small sunspot, is perturbed by a vertical or horizontal velocity pulse at the photospheric level. The type of mode generated by the pulse depends on the ratio between the sound speed c_S and the Alfvén speed v_A, on the magnetic field inclination at the location of the driver, and on the shape of the pulse in the horizontal direction. Mode conversion is observed to occur in the region in which both characteristic speeds have similar values. The fast (magnetic) mode in the region $c_S < v_A$ does not reach the chromosphere and reflects back to the photosphere at a somewhat higher layer than the $c_S = v_A$ line. This behavior is due to wave refraction, caused primarily by the vertical and horizontal gradients of the Alfvén speed. The slow (acoustic) mode continues up to the chromosphere along the magnetic field lines with increasing amplitude. We show that this behavior is characteristic for waves in a wide range of periods generated at different distances from the sunspot axis. Since an important part of the energy of the pulse is returned back to the photosphere by the fast mode, the mechanism of energy transport from the photosphere to the chromosphere by waves in sunspots is rather ineffective.

Subject headings: MHD — Sun: chromosphere — Sun: oscillations — Sun: photosphere — sunspots

Online material: color figures

1. INTRODUCTION

Sunspots show a variety of wave phenomena at different spatial and temporal scales. These phenomena are not well understood due to the complicated structure of their atmospheres. Photospheres and chromospheres above sunspots are regions in which the characteristic speeds of waves (primarily the Alfvén speed v_A) change by many orders of magnitude. The ratio between the acoustic and the Alfvén speed, c_S/v_A, decreases from much larger than 1 below the photosphere to almost zero in the corona. Waves propagate through the region where $c_S = v_A$, where mode transformation and coupling of different wave phenomena occurs. In addition, the magnetic field and background thermodynamic parameters have gradients in both the horizontal and vertical directions. The magnetic field changes its inclination from being mostly vertical at the sunspot center to being mostly horizontal at the penumbrae. All these ingredients make the modeling of waves in sunspots a rather difficult task.

In previous works, two-dimensional (2D) and three-dimensional (3D) numerical simulations of waves in the lower atmosphere in such complicated magnetic structures were carried out mostly with applications to solar network flux tubes. There is a widely developed literature on this subject in which the assumption of a "thin" flux tube is made; that is, in which the horizontal dimensions of the structure are much smaller than the characteristic vertical scales of the atmosphere (see, e.g., the recent papers by Hasan et al. 2003; Hasan & Ulmschneider 2004). The modes in thin flux tubes (kink, sausage, and torsional modes; see Spruit 1981) are different from those inside a magnetized atmosphere where the horizontal gradients are not so sharp. Waves in magnetic structures with larger horizontal dimensions were considered by, for example, Cargill et al. (1997), Rosenthal et al. (2002), Bogdan et al. (2002, 2003), and Hasan et al. (2005). The 2D studies by Rosenthal et al. (2002) and Bogdan et al. (2002, 2003) suggested an important role of the magnetic canopy. By "canopy," the authors indicate a region in which $c_S \sim v_A$ and in which different wave modes can actively interact. In particular, new wave modes can appear directly at the canopy as a consequence of mode conversion. Other important factors are the incidence angle of the waves onto the canopy and the inclination of the field there. Rosenthal et al. (2002) showed that if the inclination angle is significant, the refraction by the rapidly increasing phase speed of the fast mode can result in a total internal reflection of the waves at the $c_S = v_A$ line. According to Bogdan et al. (2003), the above effects produce the mode mixing at the $c_S = v_A$ layer. Since new modes appear at the canopy and some modes are reflected back to the lower layers and interfere with the waves coming directly from the source, the fluctuations measured in observations below and above this layer can be completely uncorrelated. If the transition between the magnetized and nonmagnetized atmosphere is sharp, as in the simulations of Hasan et al. (2005), the compressible slow magnetoacoustic waves propagate along the magnetic canopies up to the chromosphere and steepen to shocks. The fast waves are confined to the area inside the magnetic structure where $c_S < v_A$, and no fast-mode reflection is observed in these simulations.

Thus, the behavior of waves observed in a magnetic structure depends crucially on its size and magnetic field configuration. In the case of a sunspot, the horizontal variations in the field strength may not be so sharp. At the same time, the pressure, density, and temperature inside a sunspot are lower than those outside, so all the atmosphere is shifted down a few hundred kilometers (a Wilson depression). This produces important variations of the acoustic and Alfvén speeds in the horizontal directions and affects the phase speed of the propagating waves. As far as we know, no multidimensional simulations of the waves in such structures have been performed yet.

[1] Instituto de Astrofísica de Canarias, C. Vía Láctea s/n, 38205 La Laguna, Tenerife, Spain; khomenko@iac.es.

[2] Main Astronomical Observatory, National Academy of Sciences, 27 Akademika Zabolotnoho Street, 03680 Kiev, Ukraine.

Numerical models with applications to sunspots have addressed, mainly, the problems of sunspot seismology. The possibility of the existence of trapped modes of oscillations in sunspots was investigated by Bogdan & Knölker (1989), Cally & Bogdan (1993), and Cally et al. (1994). These authors considered damped oscillation modes in a vertically stratified atmosphere permeated by a constant vertical magnetic field. Horizontal gradients are ignored in this modeling. However, including these gradients will certainly change the conditions of wave reflection responsible for producing trapped oscillations and will enable new types of mode conversion. The problem of interaction of the quiet-Sun p-modes with magnetic field concentrations, i.e., scattering and absorption of the waves by sunspots, was considered in 2D simulations by Rosenthal & Julien (2000) and Cally & Bogdan (1997). The waves were assumed to come from the side of the nonmagnetic atmosphere and penetrate into the slab of a vertical magnetic field, with strength varying in the horizontal direction. The authors concluded that p-modes are partially converted into slow magnetoacoustic modes. The latter travel away from the conversion layer and thus extract energy from the quiet-Sun p-modes, which exit the slab with reduced amplitudes.

Here we investigate a different problem. One of the purposes of the simulations reported below is to help to identify the types of wave modes observed in different layers of sunspot atmospheres. Observations in spectral lines formed in the umbral photosphere reveal the existence of 5 minute oscillations with reduced amplitudes relative to the quiet Sun (see Staude 1999; Bogdan 2000; Bogdan & Judge 2006 for a review). Patches with enhanced oscillatory power have a complicated spatial distribution. There is evidence that velocity and intensity oscillations are accompanied by magnetic field oscillations with amplitudes not exceeding 10 G (e.g., Bellot Rubio et al. 2000). It is an open question as to which type of waves produces these oscillations. Higher up, the umbral chromosphere is dominated by the 3 minute oscillations. The power spectrum of the oscillations in sunspots changes gradually with height in a way such that the peak at 5 minutes disappears and a peak at 3 minutes becomes more important (see, e.g., Bogdan & Judge 2006). Recent IR observations in the 10830 Å spectral region analyzed by Centeno et al. (2006) reveal the photospheric counterpart of the 3 minute chromospheric oscillations. It was demonstrated that the power spectrum in the photosphere has a secondary peak at 3 minutes. Waves with this period propagate up to the chromosphere along the magnetic field lines. A wave train produced by a photospheric pulse typically reaches the chromosphere in 6–7 minutes, propagating with a speed of 4–5 km s^{-1}. The slow acoustic modes with periods of 3 minutes, propagating along the magnetic field lines, were also detected at higher altitudes in the transition region and corona in observations with the *Transition Region and Coronal Explorer* (*TRACE*) and the Coronal Diagnostic Spectrometer (CDS; e.g., Marsh & Walsh 2005). Thus, other questions that can be addressed by the simulations are: Do we observe the same waves at all heights? Can the photospheric perturbations propagate directly to the chromosphere and corona through the mode-mixing $c_S = v_A$ layer?

As a first step toward answering these questions, we report here the results from linear simulations of wave propagation in a magnetic sunspot-like structure. Our model sunspot is an azimuthally symmetric thick flux tube extending from the photosphere to the lower chromosphere, in magnetohydrostatic (MHS) equilibrium with the surroundings (Pizzo 1986). We assume the existence of localized sources inside a sunspot and consider the waves produced by them. On the one hand, these sources can be due to the presence of a weak convection that can generate waves directly inside the umbral atmosphere (see, e.g., Weiss et al. 1990; Cattaneo et al. 2003). On the other hand, waves can penetrate into the sunspot atmosphere from the nonmagnetic surroundings. As a first approach to the problem, we perform simulations of short-period waves; that is, waves with frequencies above the acoustic cutoff. According to investigations of mode reflection and transformation by Cally (2001), one should expect a similar behavior of the waves in the high-frequency part of the characteristic k-ω diagram. The investigation of waves with more realistic periods (3 and 5 minutes) require large computational boxes, since these waves have rather large wavelengths. As a consequence, the MHS model sunspot should extend down to the convection zone and up to the high chromosphere. For the moment, the problem of creating a realistic magnetostatic solution of the required horizontal size in these regions is not solved. Little (if anything) is known about the pressure and magnetic field distribution in sunspots in subphotospheric layers. This produces limitations for our study and justifies the use of small-period waves. Thus, the effect on the wave transformation derived from the existence of an acoustic cutoff frequency remains as a challenging subject for future investigations.

The organization of the paper is as follows. In § 2 we describe the details of the numerical calculations and the MHS model atmosphere. Sections 3, 4, and 5 give a brief review of the physics of magnetoacoustic wave propagation and transformation. Section 6 explains the results of the simulations with a localized driver. The discussion of these results is presented in § 7, and our conclusions are outlined in § 8.

2. NUMERICAL MODEL

We solve the basic ideal MHD equations, written in conservational form:

$$\frac{\partial \rho}{\partial t} + \nabla \cdot (\rho \boldsymbol{V}) = 0, \tag{1}$$

$$\frac{\partial (\rho \boldsymbol{V})}{\partial t} + \nabla \cdot \left[\rho \boldsymbol{V}\boldsymbol{V} + \left(P + \frac{\boldsymbol{B}^2}{8\pi}\right)\mathbf{I} - \frac{\boldsymbol{B}\boldsymbol{B}}{4\pi}\right] = \rho \boldsymbol{g}, \tag{2}$$

$$\frac{\partial E}{\partial t} + \nabla \cdot \left[\left(E + P + \frac{\boldsymbol{B}^2}{8\pi}\right)\boldsymbol{V} - \boldsymbol{B}\left(\frac{\boldsymbol{B}\cdot\boldsymbol{V}}{4\pi}\right)\right] = \rho \boldsymbol{V}\cdot\boldsymbol{g} + \rho Q, \tag{3}$$

$$\frac{\partial \boldsymbol{B}}{\partial t} = \nabla \times (\boldsymbol{V} \times \boldsymbol{B}), \tag{4}$$

where $\mathbf{I}$ is the diagonal identity tensor and E is the total energy,

$$E = \frac{1}{2}\rho V^2 + \frac{P}{\gamma - 1} + \frac{B^2}{8\pi}. \tag{5}$$

All other symbols have their usual meaning. The term ρQ, on the right-hand side of equation (3), contains the energy losses. The code can take into account the energy losses due to radiative cooling. However, for simplicity, here we consider adiabatic waves.

To close the system, the equation of state of the perfect gas is used. No changes in the mean molecular weight due to ionization are taken into account.

As a first step in our modeling, we linearize the equations before solving them. By doing so, the solutions of the system cannot reach a shock wave regime. Thus, our simulations are valid

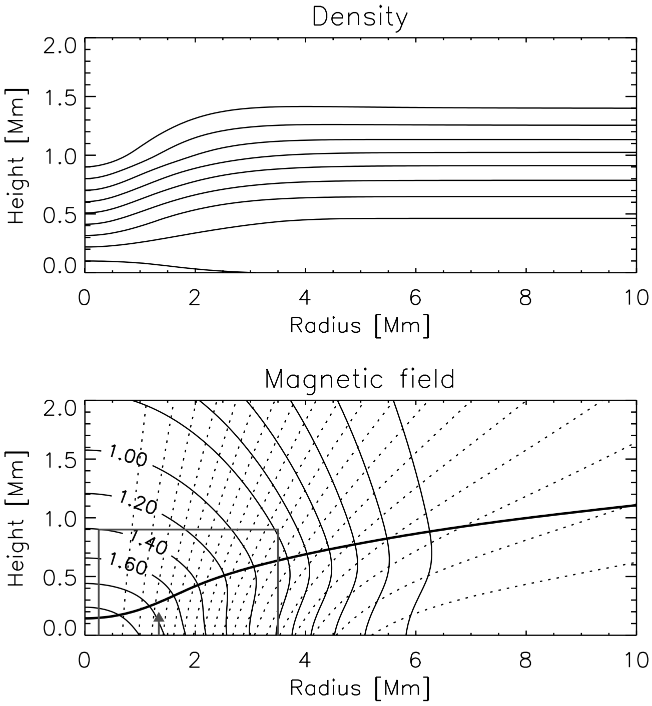

FIG. 1.—*Top*: Contours of constant log ρ for the MHS solution. The density deficit associated with the Wilson depression is evident. *Bottom*: Contours of constant $|B|$. The labels indicate the magnetic field strength in units of kG. The thick line denotes the surface at which $v_A = c_S$. The dotted lines indicate magnetic field lines. The gray box corresponds to the domain taken for the dynamical simulations and the gray arrow indicates the location of the driver. Note that, for the sake of clarity, the vertical axis has been expanded, giving an appearance of reduced inclination of the magnetic field lines. [*See the electronic edition of the Journal for a color version of this figure*.]

for the photosphere and the low chromosphere, where observations demonstrate that the waves are still linear (Bogdan 2000).

2.1. *Magnetohydrostatic Equilibrium*

To be able to linearize the system (eqs. [1]–[4]) and obtain equations for small perturbations to the equilibrium state, one has to evaluate the MHS solution of the system. Thus, the following equations of the equilibrium force balance have to be solved:

$$-\nabla P_0 + \rho_0 \boldsymbol{g} + \frac{1}{4\pi}(\nabla \times \boldsymbol{B}_0) \times \boldsymbol{B}_0 = 0, \qquad (6)$$

$$\nabla \cdot \boldsymbol{B}_0 = 0, \qquad (7)$$

where the subscript "0" stands for the equilibrium value of the atmospheric parameters.

We followed the strategy described in Pizzo (1986) and numerically solved the system of MHS equations (eqs. [6]–[7]) in cylindrical coordinates. As a first step, a potential field distribution was generated. A specific form of the vertical magnetic field component was assumed at the lower photospheric boundary:

$$B_z(r, z = 0) = B_0 \exp\left[-(r/r_e)^2\right]. \qquad (8)$$

Here the parameter r_e is a scaling for magnetic field variations. For the model considered below, we took r_e to be equal to 3 Mm. At the left boundary (the sunspot axis) the field is vertical, and the top and the right boundaries are sufficiently far away to ensure that the conditions there do not influence the interior solution. Once the potential field solution is obtained, we specify a pressure distribution along the magnetic field lines. For this purpose, two boundary conditions are used: the semiempirical model atmosphere of Avrett (1981) at the sunspot axis, and the field-free model atmosphere of Spruit (1974) and used in VALC (Vernazza et al. 1981) at the boundary far from the axis. These two model atmospheres are shifted in height z with respect to each other according to a prescribed Wilson depression. Some smooth transition between the internal and the external pressure distributions is calculated. Given the approximations for the magnetic field and pressure, the equations of force balance are iterated until convergence is reached. For the details of the calculations, see Pizzo (1986).

Figure 1 illustrates the basic properties of the MHS solution. Some characteristic parameters of the model are also given in Table 1. Our model sunspot is a thick flux tube. It is assumed to be azimuthally symmetric and to have no twist. It belongs to a category of distributed-current models; that is, the variations of field strength and gas pressure are continuous across the spot. The characteristic size of this flux tube is about 6 Mm. However, there is no sharp transition between umbra and penumbra, or between penumbra and field-free photosphere. The inclination of the field lines changes gradually from the sunspot axis outward. The magnetic field at the axis is about 2200 G at $z = 0$ km and decreases with height. The thermodynamic properties of the solution are rather complex. In the case shown in Figure 1, the $\log \tau_5 = 0$ level is 350 km deeper at the sunspot axis than at the outside photosphere.

Figure 2 gives the distribution of the characteristic speeds across the model sunspot. The temperature stratification is neither isothermal nor polytropic, but is rather close to the real stratification in the sunspot photosphere and chromosphere of the Sun. Thus, the sound speed distribution shows both horizontal and vertical variations. The distribution of the Alfvén speed is influenced by the density change across the sunspot radius that is due to the Wilson depression. The Alfvén speed changes by

TABLE 1
CHARACTERISTIC PARAMETERS OF THE MODEL SUNSPOT

	Sunspot Axis		4000 km from Axis	
Parameter	z = 0 km	z = 800 km	z = 0 km	z = 800 km
Temperature (K)	3430	2630	7760	2600
Magnetic field (G)	2170	1440	740	760
Inclination (deg)	0	0	48	53
Sound speed (km s^{-1})	8	7	12	7
Alfvén speed (km s^{-1})	5	300	2	18
c_S^2/v_A^2	2	0.0005	30	0.15
Pressure scale height (km)	135	105	310	105

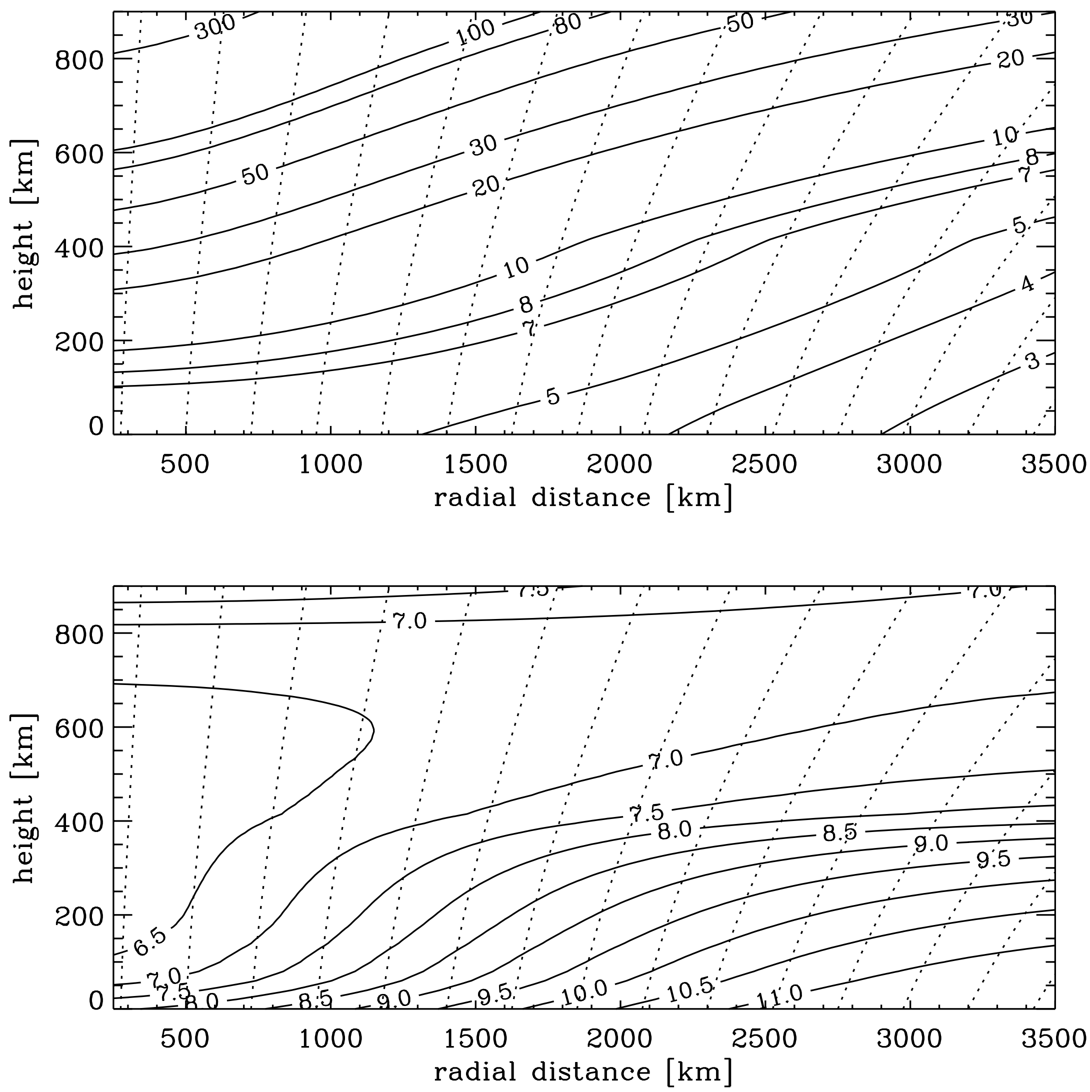

FIG. 2.—*Top*: Contours of constant v_A for the MHS solution. *Bottom*: Contours of constant c_S. Note the strong horizontal gradients of both v_A and c_S due to the Wilson depression. The dotted lines indicate magnetic field lines. The size of the domain shown is the same as that of the gray box in Fig. 1.

orders of magnitude both in the horizontal and vertical directions. The fast change of v_A is the main reason for the variations of the ratio between the acoustic and Alfvén speeds that can be seen in Figures 1 and 2. The height of the level at which both characteristic speeds are equal increases with increasing distance to the sunspot axis.

The gray box in Figure 1 corresponds to the domain used in the dynamical simulations. The gray arrow indicates the location of the driver for the simulations described below. Note that in all figures in this paper the $z = 0$ level is assumed with respect to the sunspot axis.

2.2. *Details of the Calculations*

The MHS equilibrium model was transformed from cylindrical coordinates (r, ϕ, z) into a 3D Cartesian cube. In a general case, all three components of the magnetic field vector are nonzero in Cartesian coordinates. After the transformation, we obtained the background model atmosphere parameters P_0, ρ_0, B_{x0}, B_{y0}, and B_{z0} that depend on x, y, and z.

Given the MHS model atmosphere, we solved the linearized system (eqs. [1]–[4]) in Cartesian coordinates under the following conditions. We used a 2.5-dimensional (2.5D) approach. This implies that all first-order quantities are taken to depend only on the x and z spatial coordinates, but the background zeroth-order parameters are allowed to have variations also in the third, y, direction. We chose the slice of the azimuthally symmetric model sunspot in which the B_y component of the field is equal to zero. Thus, the waves launched in this plane under the 2.5D approximation will remain inside it during the entire computational time. By adopting this approach, we excluded Alfvén waves from consideration.

All spatial derivatives are discretized using fourth-order centered differences on a five-point stencil. The time stepping is explicit, using a fourth-order Runge-Kutta scheme. The computational box used for dynamical simulations extends 0.86 Mm in the vertical direction and 3.5 Mm in the horizontal direction. The bottom level corresponds to $z = 0$ at the axis of the sunspot umbra photosphere. The numerical resolution of the simulations is $\Delta z = 5$ km and $\Delta x = 12.5$ km in the vertical and horizontal directions, respectively. To stabilize the code and reduce high-frequency variations on scales unresolved by the numerical scheme, we included artificial diffusion terms in equations (1)–(4) following the strategy described in Vögler et al. (2005). The diffusion coefficients were kept as small as possible to ensure that the numerical diffusion did not affect the solution to a large extent.

2.3. *Boundary Conditions*

In numerical simulations with an open domain it is crucial to have accurate nonreflecting boundary conditions. The most widely used nonreflecting boundary conditions for the Euler equations are the characteristic-based boundary conditions (Hirsch 1990). However, in multidimensional simulations and in the presence of a magnetic field with a complicated structure, the calculation of the characteristic directions becomes a serious problem. In addition, the solar atmosphere is strongly stratified in the vertical direction, which leads to an unavoidable numerical reflection of the slow (acoustic) mode at the upper boundary of the simulation domain.

In our numerical model we applied nonreflecting boundary conditions based on an absorbing 2D perfectly matched layer (PML; Berenger 1994, 1996; Hu 1996; Qi & Geers 1998; Hu 2001). Initially the PML boundary formalism was developed for simulations of electromagnetic waves (see Berenger 1994) and in aeroacoustics (Qi & Geers 1998). Recently PML boundary conditions were successfully applied to simulations of acoustic waves in a strongly stratified solar convection zone (Parchevsky & Kosovichev 2005). The basic idea consists of splitting the Euler equations, written in conservational form as

$$\frac{\partial \boldsymbol{U}}{\partial t}+\frac{\partial \boldsymbol{F}(\boldsymbol{U})}{\partial x}+\frac{\partial \boldsymbol{G}(\boldsymbol{U})}{\partial z}=\boldsymbol{H}(\boldsymbol{U}), \tag{9}$$

into a set of equations in the PML domain that contain just a single spatial derivative. Artificial damping terms are added to the split equations in the PML domain:

$$\frac{\partial \boldsymbol{U}_1}{\partial t}+\frac{\partial \boldsymbol{F}(\boldsymbol{U})}{\partial x}+\sigma_x \boldsymbol{U}_1=\boldsymbol{H}_1(\boldsymbol{U}), \tag{10}$$

$$\frac{\partial \boldsymbol{U}_2}{\partial t}+\frac{\partial \boldsymbol{G}(\boldsymbol{U})}{\partial z}+\sigma_z \boldsymbol{U}_2=\boldsymbol{H}_2(\boldsymbol{U}). \tag{11}$$

Here $\boldsymbol{U}_1$ and $\boldsymbol{U}_2$ sum to $\boldsymbol{U}$, and $\boldsymbol{H}_1(\boldsymbol{U})$ and $\boldsymbol{H}_2(\boldsymbol{U})$ sum to $\boldsymbol{H}(\boldsymbol{U})$. The vector $\boldsymbol{U}$ contains the conserved variables ρ, $\rho\boldsymbol{V}$, $\boldsymbol{B}$, and E; $\boldsymbol{F}$ and $\boldsymbol{G}$ are the corresponding fluxes; and $\boldsymbol{H}$ represents the right-hand side of equations (1)–(4). The absorption coefficient, σ_x, is nonzero only at the x interface (left and right boundaries), and σ_z is nonzero at the z interface (top and bottom boundaries).

It has been shown that, theoretically, the PML has no reflection for plane waves incident on a flat interface for all frequencies, independent of the incidence angle. However, in the finite-difference implementation of the PML equations, a certain amount of numerical reflection may occur due to sharp variations of the absorption coefficients at the interface (Berenger 1996). To avoid this, a smooth variation of σ_x and σ_z, increasing from small values at the PML interface to a large value at the outer boundary, is implemented in the numerical solution (Hu 2001):

$$\sigma_x=\frac{a}{\Delta x}\left(\frac{x-x_{\rm PML}}{x_{\rm PML}}\right)^2,$$
$$\sigma_z=\frac{b}{\Delta z}\left(\frac{z-z_{\rm PML}}{z_{\rm PML}}\right)^2, \tag{12}$$

where Δx and Δz are the discretization steps, a and b are amplitudes, and $x_{\rm PML}$ and $z_{\rm PML}$ are the thickness of the PML domain in both spatial directions. The optimum thickness of the layer is found to be 8–10 grid points. We added a PML at the left, right, and top boundaries of our simulation domain.

2.4. *Photospheric Driver*

At the bottom (photospheric) boundary, we specified either a vertical or horizontal velocity as a function of time and horizontal coordinate x:

$$V_{1x,z}(x,\,t)=V_0\sin(\omega t)\exp\left[-(x-x_0)^2/2\sigma^2\right]. \tag{13}$$

The perturbation is localized in the x-axis and has a Gaussian shape in this direction. In the simulations described here, the pulse is located at a distance $x_0 = 1300$ km from the sunspot axis (see Fig. 1). The MHS model sunspot does not extend enough in the horizontal and vertical directions to make the study of waves in the 3–5 minute regime possible. Such waves are expected to have large spatial wavelengths and will not fit into the simulation domain. For the moment, it is an open problem to create a stable MHS solution of the required size. For this reason, we focus our study on shorter period waves. According to the investigations of wave propagation in a magnetized atmosphere (Zhugzhda & Dzhalilov 1982; Cally 2001), one should expect a similar behavior of waves in the high-frequency part of the k-ω diagram above the acoustic cutoff (that is, in principle, one should not expect qualitative differences between the waves of, say, 10 and 100 s periods). Having this in mind, we choose a period of 10 s for the driver. This allows us to use a rather small spatial wavelength for the oscillations and to observe clearly the wave refraction and transformation. The results of these simulations are discussed in § 6. For comparison, in § 7 we show briefly the simulations with a 50 s period driver. The spatial extent of the driver is $\sigma = 62.5$ km for the 10 s simulations and $\sigma = 250$ km for the 50 s simulations. The initial wave amplitude, V_0, at $z = 0$ was taken to be equal to 200 m s^{-1}.

In addition, we carried out simulations with an instantaneous pressure pulse as an initial condition. In this case, the initial perturbation has the form

$$P_1(x,\,z)\sim\exp\left[-(x-x_0)^2/2\sigma_x^2\right]\exp\left[-(z-z_0)^2/2\sigma_z^2\right] \tag{14}$$

and is only present at the first time moment. The parameters σ_x and σ_z are equal to 62.5 and 25 km, respectively, and the pulse is located at $x_0 = 1300$ km and $z_0 = 100$ km. In these simulations, a PML layer was also added at the lower photospheric boundary. The results of these simulations are used in § 7.

3. CONCEPTS OF MODE TRANSFORMATION

As follows from Figure 1, a wave propagating from the photosphere to the chromosphere will encounter a layer in which both characteristic speeds are equal, $v_{\rm A} = c_S$. At the vicinity of this layer, the different wave modes can interact, and mode transformation takes place (see, e.g., Zhugzhda & Dzhalilov 1982, 1984; Bogdan et al. 2002, 2003; Rosenthal et al. 2002; Cally 2005, 2006). To better understand the results of the numerical simulations, we briefly review the concepts of mode transformation here.

The phase speed, $V_{\rm ph}$, of a wave is a continuous function of the spatial coordinates and must be preserved after the mode transformation. Approaching the transformation layer, $v_{\rm A} \approx c_S$, the phase speeds of the modes become close, and the energy can be partially transferred between the different branches of the dispersion relation. The direction and the effectiveness of the transformation depend, among other parameters, on the wave frequency

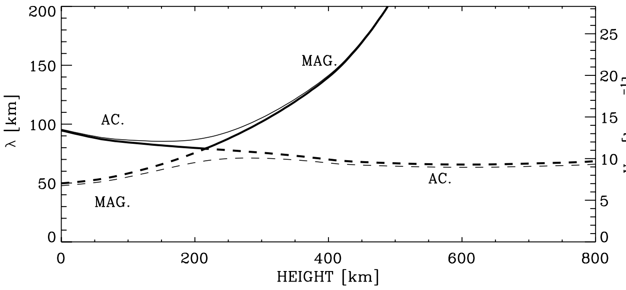

FIG. 3.—Wavelength/phase speed of the fast and slow modes as a function of height, calculated under the approximation of a locally homogeneous atmosphere with a uniform magnetic field. Thin lines indicate oblique propagation (***k*** is directed along the vertical). Thick lines indicate longitudinal propagation (both ***k*** and $\boldsymbol{B}_0$ are inclined by 14° with respect to the vertical at the $v_{\rm A} = c_S$ line). Solid lines indicate the fast mode; dashed lines indicate the slow mode.

and the attack angle between the wavevector ***k*** and the magnetic field.

In the case in which the directions of the wavevector ***k*** (defined locally) and the field vector $\boldsymbol{B}_0$ are not very different in the $v_{\rm A} \approx c_S$ region (when the angle ψ between both directions is small), the fast mode can be partially transformed into the slow mode and vice versa. In this transformation, the wave preserves its physical nature (magnetic or acoustic). After the transformation, the wave switches to another branch of the dispersion curve. In the case of high-frequency (above the acoustic cutoff) oscillations in a vertical magnetic field, the transformation coefficient from the fast to slow mode is given by the following approximate formula (Cally 2006):

$$C = \exp\left[-\frac{k\pi \sin^2\psi}{\left|(d/ds)\left(c_S^2/v_{\rm A}^2\right)\right|}\right], \tag{15}$$

where s is the arclength along the direction defined by the vector ***k***. The coefficient should be evaluated at the point where $c_S = v_{\rm A}$. This equation can be interpreted in the following way. The fast-to-slow mode conversion is complete for the waves with ***k*** directed along $\boldsymbol{B}_0$. For $\psi \neq 0$, the part of the energy that goes from the fast branch into the slow branch of the dispersion relation decreases with increasing attack angle. The value of C depends on the wave frequency through the wavenumber k. The higher the frequency, the smaller is the cone of values of ψ for which the fast-to-slow mode conversion is effective.

If the angle that forms the wavevector ***k*** with the magnetic field is arbitrary but not zero, the fast solution below the $v_{\rm A} \approx c_S$ region can continue as a fast solution above this region. The same is true for the slow solution. Physically, it means that the fast mode remains fast through the whole atmosphere, even if the ratio between the characteristic velocities changes. In this transformation the nature of the fast mode switches from acoustic ($v_{\rm A} < c_S$) to magnetic ($v_{\rm A} > c_S$). In the same way, a slow mode remains slow, changing from magnetic to acoustic. According to Cally (2005), the fast-to-fast mode conversion coefficient increases with increasing angle of ψ and increasing frequency of the wave, ω. For the waves with ***k*** directed along the field ($\psi = 0$), the conversion coefficient is zero independent of the wave period, and no energy is transferred from the acoustic to the magnetic mode and vice versa (recall that the fast-to-slow mode conversion in this case is complete; see eq. [15]).

In view of these concepts, Figure 3 gives an idea of the possible mode transformations that can occur for linear magnetoacoustic waves in the particular case of our model sunspot. It shows the phase speeds and wavelengths ($\lambda = 2\pi/k$) of the fast and slow modes as a function of height. In the high-frequency limit, when the effect of the acoustic cutoff is unimportant (which is justified for the wave periods used in the simulations), we can roughly estimate $V_{\rm ph}$ from the dispersion relation for waves in a homogeneous unstratified atmosphere ($\boldsymbol{g} = 0$) with a uniform magnetic field:

$$V_{\rm ph}^2 = \frac{\omega^2}{k^2} = \frac{1}{2}\left(c_S^2 + v_{\rm A}^2\right) \pm \frac{1}{2}\sqrt{\left(c_S^2 + v_{\rm A}^2\right)^2 - 4c_S^2 v_{\rm A}^2 \cos^2\psi}, \tag{16}$$

where the plus sign indicates the fast mode, while the minus sign indicates the slow mode. To compute the curves given in Figure 3, we have introduced in equation (16) the local values of the atmospheric parameters from the MHS model atmosphere at $x = 1300$ km, with z varying from 0 to 800 km; that is, at the location of the pulse. The $v_{\rm A} = c_S$ layer is located at $z \approx 230$ km. The figure shows that, in the case in which ***k*** is not parallel to $\boldsymbol{B}_0$ (*thin lines*), the phase speeds of the fast and slow modes are not the same at any height (although the difference between them is small at the transformation layer). If ***k*** and $\boldsymbol{B}_0$ are parallel at the $v_{\rm A} = c_S$ line, the phase speeds of both modes are exactly the same (see the two thick lines in Fig. 3, which cross each other at $z \approx 230$ km). In this particular example, both vectors ***k*** and $\boldsymbol{B}_0$ are inclined by about 14° with respect to the vertical at the height where $v_{\rm A} = c_S$. Since $\psi = 0$ in this case, according to equation (15) (see Cally 2006), the fast-to-slow (or slow-to-fast) mode conversion will be complete. An estimation from equation (15) for the values of c_S and $v_{\rm A}$ as in Figure 2 gives that a change of ψ by 5°–7° (for the 10 s period wave) and by about 15° (for the 50 s period wave) produces a drop of C from 1 to 0.5. Thus, in the case of small deviations from the longitudinal propagation, the fast-to-slow mode conversion is not complete. The fast-to-fast and slow-to-slow mode conversions are possible in all other cases, with the conversion coefficient increasing with increasing inclination of ***k***. Such transformations are never complete, and some energy can always escape from the fast into the slow mode and vice versa. Its amount becomes negligible for large ψ.

4. DIRECTION OF WAVE PROPAGATION

Even in the absence of gradients of $v_{\rm A}$ or c_S and inclination of the magnetic field lines, θ, the phase speed of both the fast and slow modes depends on their direction of propagation, locally defined by ***k***. In this sense, the atmosphere can be considered as an anisotropic medium. In this type of medium, the directions of the phase and group velocities generally do not coincide. The direction of the phase velocity is defined by the vector ***k*** (the surface with constant phase is perpendicular to ***k*** by definition). The energy of the wave in an anisotropic medium propagates in the direction of its group velocity, $\boldsymbol{v}_g = \partial\omega/\partial\boldsymbol{k}$ (Landau & Lifshitz 1984). Hereafter, by the direction of the wave propagation, we mean the direction of $\boldsymbol{v}_g$.

For simplicity, consider the case of waves in a homogeneous unstratified medium with a uniform magnetic field. The dispersion relation of the fast and slow modes in this case is given by equation (16). In the limit when one of the characteristic speeds is much larger than the other, equation (16) can be simplified to give

$$\begin{aligned} \omega &\approx k c_S \quad (v_{\rm A} \ll c_S), \\ \omega &\approx k v_{\rm A} \quad (v_{\rm A} \gg c_S) \end{aligned} \tag{17}$$

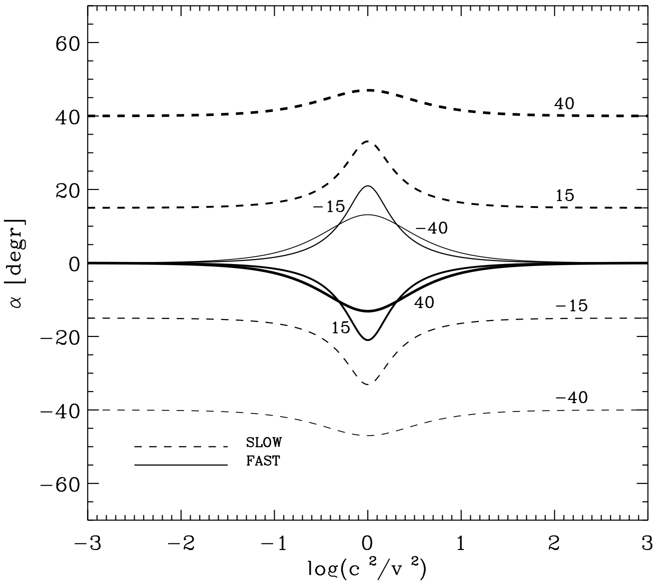

FIG. 4.—Angle between the directions of $\boldsymbol{v}_g$ and $\boldsymbol{k}$, calculated under the approximation of a locally homogeneous atmosphere with a uniform magnetic field, as a function of the ratio between the two characteristic speeds. The lines with different thicknesses correspond to different angles ψ between $\boldsymbol{k}$ and $\boldsymbol{B}_0$ (marked on the figure). Solid lines indicate the fast mode; dashed lines indicate the slow mode.

for the fast mode and

$$\omega \approx k v_{\rm A} \cos\psi = v_{\rm A} \frac{\boldsymbol{k} \cdot \boldsymbol{B}_0}{|B_0|} \quad (v_{\rm A} \ll c_S),$$
$$\omega \approx k c_S \cos\psi = c_S \frac{\boldsymbol{k} \cdot \boldsymbol{B}_0}{|B_0|} \quad (v_{\rm A} \gg c_S) \qquad (18)$$

for the slow mode. Since, in the case of the fast mode, the expression for ω (eq. [17]) is independent of $\boldsymbol{k}$, the group velocity is equal to either c_S or $v_{\rm A}$, and its direction is that of $\boldsymbol{k}$. The directions of the phase and group velocities coincide, and the medium can be considered isotropic for a fast wave in this regime. In the case of the slow mode, $\boldsymbol{v}_g$ is directed along the vector $\boldsymbol{B}_0$. Thus, in both cases ($v_{\rm A} \gg c_S$ or $v_{\rm A} \ll c_S$), the fast mode will propagate in the direction of $\boldsymbol{k}$, and the slow mode will be directed along the magnetic field lines.

In the intermediate case, when $v_{\rm A} \approx c_S$, the atmosphere is anisotropic for both modes, and the direction of the group velocities is different from that of the phase velocities; that is, the vector $\boldsymbol{v}_g$ is inclined by some angle with respect to the vector $\boldsymbol{k}$. The expression for $\boldsymbol{v}_g$ can be derived analytically from the dispersion relation, equation (16), by calculating the derivative of ω with respect to $\boldsymbol{k}$. The angle between the two directions, α, depends on the local values of $v_{\rm A}$ and c_S and the angle, ψ, between the direction of the magnetic field and $\boldsymbol{k}$. It is given by the following equation:

$$\tan\alpha = \frac{c_S^2 v_{\rm A}^2 \sin 2\psi}{2V_{\rm ph}^2\left(2V_{\rm ph}^2 - v_{\rm A}^2 - c_S^2\right)}, \qquad (19)$$

where $V_{\rm ph}$ is defined by equation (16). The inclination angles of $\boldsymbol{v}_g$ for both modes calculated for different values of ψ are displayed in Figure 4 as a function of the ratio between $v_{\rm A}$ and c_S.

Figure 4 helps to summarize all the reasoning expressed above. It shows that $\boldsymbol{v}_g$ is not, in general, parallel to either $\boldsymbol{k}$ or $\boldsymbol{B}_0$. In the limit when $v_{\rm A}$ is either $\gg c_S$ or $\ll c_S$, the slow mode propagates longitudinally along $\boldsymbol{B}_0$, in agreement with equation (18). The fast mode propagates along $\boldsymbol{k}$, in agreement with equation (17). When approaching the $v_{\rm A} \approx c_S$ region, $\boldsymbol{v}_g$ deviates, for both modes, from these directions. The maximum deviation is achieved for $v_{\rm A} = c_S$ and $\psi = 0$ and is 27° for both modes (see Osterbrock 1961). The angle that $\boldsymbol{v}_g$ makes with $\boldsymbol{B}_0$, for the *slow* mode, has the same sign as ψ, while, for the fast mode, the angle that $\boldsymbol{v}_g$ makes with $\boldsymbol{k}$ has the sign opposite to ψ. The angle between the directions of propagation of the *fast* and *slow* mode increases when the characteristic speeds are close and is at maximum at the $v_{\rm A} = c_S$ line.

5. WAVE REFRACTION

In a stratified inhomogeneous atmosphere, there is another factor that can change the direction of propagation of waves. In the limits when $v_{\rm A} \gg c_S$ or $v_{\rm A} \ll c_S$, both the phase and group velocities of the fast mode are independent of the direction. In this situation, the gradients of the characteristic speeds start playing an important role and modify the direction of propagation of the fast mode due to refraction. The fast-wave refraction can be understood in terms of geometric optics. The direction of propagation of a plane wave impinging on an interface between two media with different indices of refraction (or phase speeds) will change according to Snell's law of refraction,

$$\frac{\sin i}{\sin r} = \frac{V_{{\rm ph},i}}{V_{{\rm ph},r}}, \qquad (20)$$

where i and r are the incidence and refraction angles, respectively. In our case, the reference interfaces are the contours of $v_{\rm A} = $ constant when $v_{\rm A} \gg c_S$ or the contours of $c_S = $ constant in the opposite limit. The direction of the fast-mode refraction depends on the incidence angle, i, on this interface. In the limit of $v_{\rm A} \gg c_S$, the line that separates waves refracting to the right from those refracting to the left is the $\nabla v_{\rm A}$ line. This line is perpendicular to the contours of $v_{\rm A} = $ constant at every height. The maximum height reached by the wave with an initial direction i_0 can be found from the condition $\sin i_0 = V_{{\rm ph},i_0}/V_{{\rm ph},r}$ (Osterbrock 1961).

Consider the particular case of the atmosphere shown in Figure 2. Suppose a plane wave starts propagating in the region $v_{\rm A} \gg c_S$. The $\nabla v_{\rm A}$ line in our model atmosphere is inclined to the left with respect to the vertical by about 14°. Thus, we may expect that waves with the wavevector $\boldsymbol{k}$ inclined by less than −14° with respect to the vertical will be refracted toward the axis, while those with $\boldsymbol{k}$ inclined more than −14° will be refracted away from the axis. The height where complete reflection occurs depends on the incidence angle i_0, and, in any case, it is expected to be located well above the height where $v_{\rm A} = c_S$ (at 500–1000 km, depending on the distance from the axis; see Fig. 1).

6. ANALYSIS OF THE SIMULATIONS

Figures 5, 6, 7, and 8 show the results of the numerical solution of the linearized equations (1)–(4) with a vertical (Figs. 5 and 6) and horizontal (Figs. 7 and 8) driver and a 10 s period. There are several factors that define a set of dominant wave modes in the simulations: the inclination of the magnetic field lines at the location of the driver, the ratio between $v_{\rm A}$ and c_S, and the horizontal shape of the pulse in the x direction.

Since the amplitude of the pulse is not constant in x (see eq. [13]), it necessarily gives rise to a set of slow or fast magnetoacoustic modes with different horizontal wavenumbers k_x. The amplitudes of different harmonics can be obtained after the Fourier

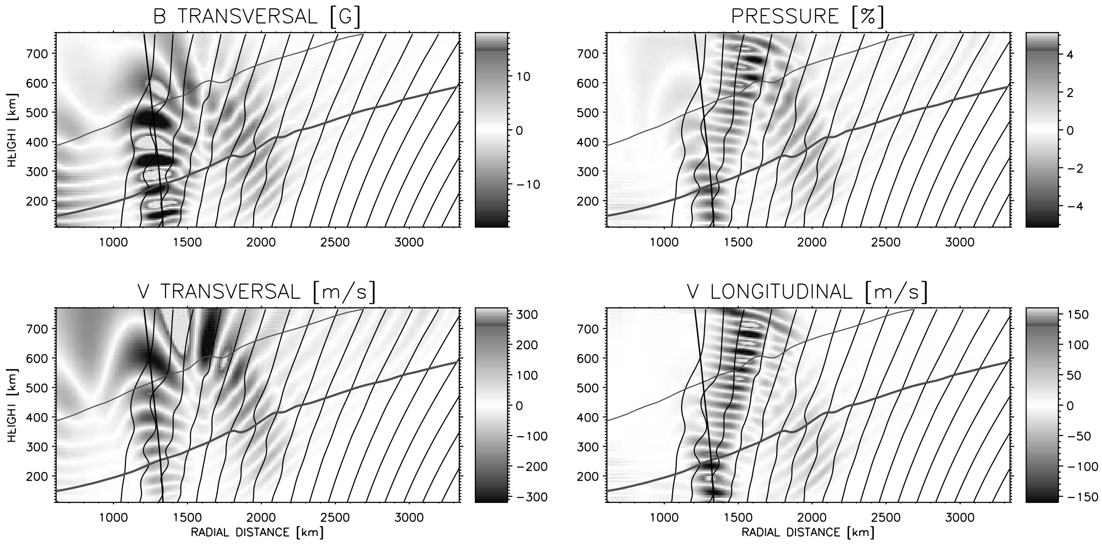

FIG. 5.—Variations of the velocity, magnetic field, and pressure at an elapsed time $t = 100$ s after the beginning of the simulations, for the vertical driving with a 10 s period. In each panel, the horizontal axis represents the radial distance x from the sunspot axis. The black inclined lines indicate magnetic field lines. The two gray lines indicate contours of constant c_S^2/v_A^2, with the thicker line corresponding to $v_A = c_S$ and the thinner line to $c_S^2/v_A^2 = 0.1$. The black thick line inclined to the left indicates the direction of ∇v_A, starting at the location of the pulse. *Top left*: Transversal variations of the magnetic field. *Top right*: Relative pressure variations. *Bottom*: Transversal and longitudinal variations of the velocity. [*See the electronic edition of the Journal for a color version of this figure*.]

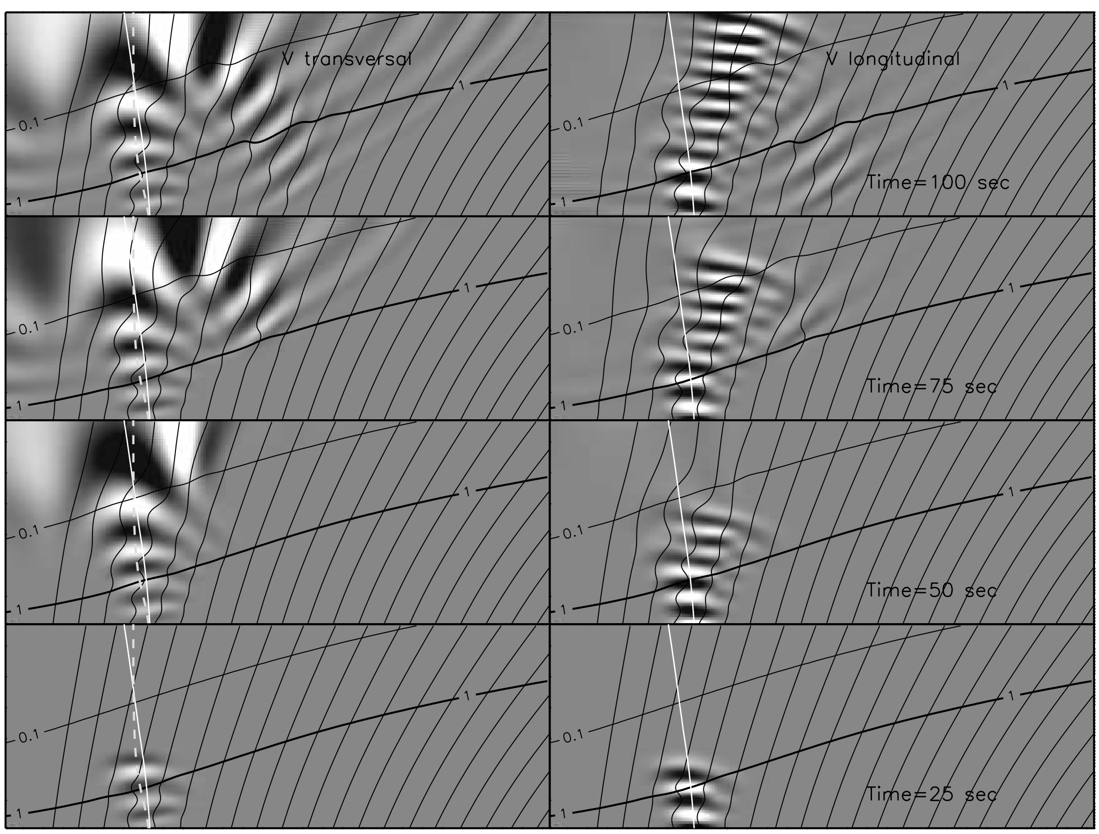

FIG. 6.—Time evolution of the longitudinal and transversal velocity components for the 10 s vertical driving simulations. The black thin inclined lines are magnetic field lines. The white solid line indicates the direction of ∇v_A, starting at the location of the pulse. The white dashed line indicates the direction of energy propagation, given by $\boldsymbol{v}_g$. The two black lines marked with numbers are contours of constant c_S^2/v_A^2, with the thicker line corresponding to $v_A = c_S$ and the thinner line to $c_S^2/v_A^2 = 0.1$. The size of the domain is the same as in Fig. 2.

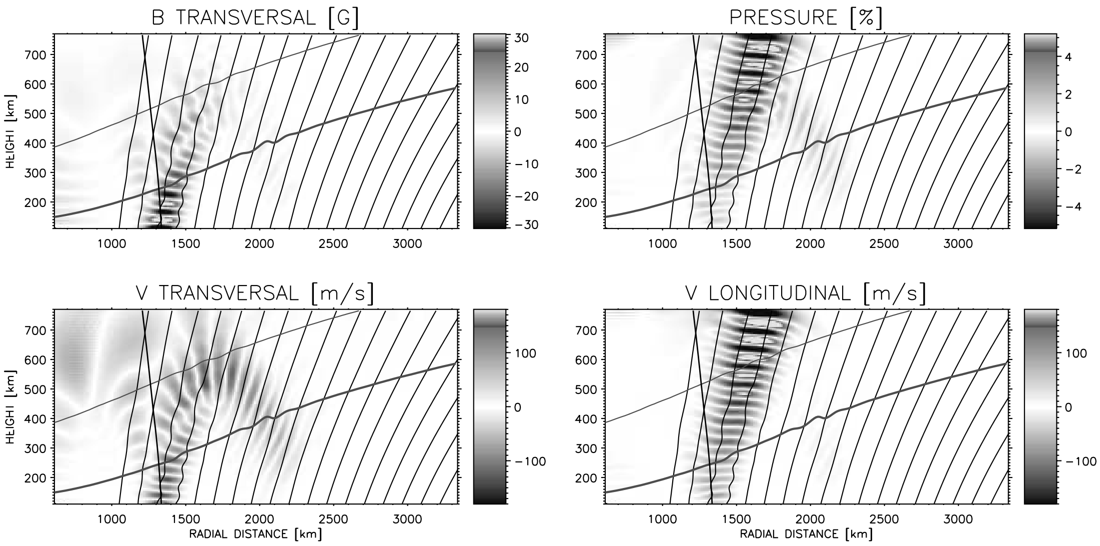

FIG. 7.—Variations of the velocity, magnetic field and pressure at an elapsed time $t = 100$ s after the beginning of the simulations for the horizontal driving with a 10 s period. The format of the figure is the same as that of Fig. 5. [*See the electronic edition of the Journal for a color version of this figure.*]

transformation of the Gaussian describing the pulse in the x direction. They are described by the following equation (except for a constant coefficient):

$$A_x \sim \exp\left(-k_x^2 \sigma_x^2/2\right). \tag{21}$$

Thus, the amplitude of the Fourier component decreases with increasing absolute value of its horizontal wavenumber. Those modes with the vector $\boldsymbol{k}$ directed along the vertical ($k_x = 0$) have more weight. As we will see later, depending on the value of k_x, each mode follows a different path in the x-z plane and can experience a different transformation at the $v_\mathrm{A} = c_S$ layer.

The slow and fast magnetoacoustic modes can be separated by means of plotting the longitudinal and transversal components of the velocity variations with respect to the background magnetic field at every point. However, the distinction between the modes can only be made clear in the $v_\mathrm{A} \gg c_S$ or $v_\mathrm{A} \ll c_S$ regions, where either the magnetic field or the gas pressure strongly dominates

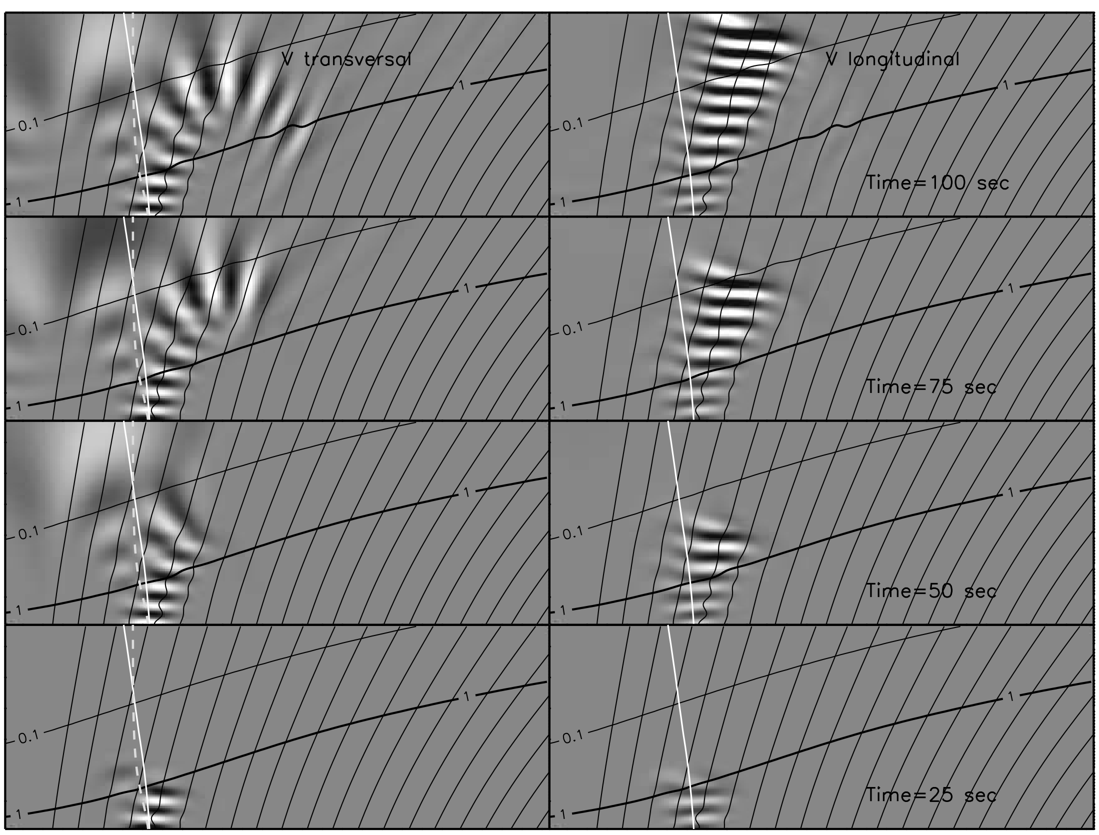

FIG. 8.—Time evolution of the longitudinal and transversal velocity components for the 10 s horizontal driving simulations. The format of the figure is the same as that of Fig. 6.

the dynamics. In the $v_A \gg c_S$ limit, the slow magnetoacoustic mode is visible in the longitudinal velocity and in the pressure variations. The fast mode is visible in the transversal velocity, as well as in the variations of the magnetic field vector. In the $v_A \ll c_S$ limit, the opposite is true.

6.1. *Vertical Driving*

The vertical velocity pulse located at the lower boundary in the $v_A < c_S$ region generates a set of fast (acoustic) modes with different values of k_x (see Figs. 5 and 6). Since the field orientation at the location of the driver is not vertical ($\theta \approx 13°$), some of the energy of the pulse also goes into the slow (magnetic) mode. However, due to the small field inclination, its amplitude is significantly weaker than that of the fast mode.

The fast mode propagating in a nonvertical field causes perturbations in both the longitudinal and transversal components of the velocity. The amplitude of the longitudinal velocity variations is larger than that of the transversal ones (compare the bottom panels in Fig. 5). Due to the presence of waves with different values of k_x, the initial perturbation expands in the horizontal direction as it propagates upward. The perturbations in the longitudinal and transversal velocity reach the $v_A = c_S$ level almost simultaneously (Fig. 6, *bottom*). In addition, as the fast wave propagates across the magnetic field lines, it produces variations in the background pressure, magnetic field strength, and its inclination. In order to make the magnetic field line variations visible in Figure 5 (*top left*), we have amplified the $\boldsymbol{B}_1$ vector by multiplying it by an adequate factor. Input velocity variations with amplitudes of $\sim$200 m s^{-1} cause magnetic field variations of 10–20 G and pressure variations of 5% from the MHS value. As follows from Figure 3, the local wavelength of the fast mode at $z = 0$ km is $\sim$2 times larger than that of the slow mode and is $\approx$100 km. This number coincides with the wavelength of the fast mode obtained from numerical simulations. Note that the magnetic field and pressure perturbations have the same vertical wavelength. This proves that both are produced by the same fast mode.

In the $v_A > c_S$ region, several modes propagating in different directions can be observed. As follows from Figure 6, after reaching the $v_A = c_S$ line, the transversal and longitudinal velocity variations have clearly different propagation speeds. At an elapsed time of 50 s, the transversal velocity perturbation reaches the top of the domain, while the longitudinal velocity only reaches half of it. The wavelengths of the perturbations are also very different.

Keeping in mind the results from § 3, it is easy to understand the mode transformations that take place in this simulation. We can observe two mode transformations at the $v_A \approx c_S$ region. The first transformation is the fast (acoustic) mode with $k_x \approx 0$ at $z = 0$ km, which is transformed into the fast (magnetic) mode in the $v_A > c_S$ region. More strictly, in this case (as well as in all the cases described below) one should speak about the set of modes with values of k_x that vary in a certain range around the given value. The behavior of these waves (their path in the *x-z* plane; conversion coefficients) differs only slightly, and the wave train formed by them can be considered roughly as a monochromatic wave. Thus, below we describe the wave behavior by referring just to a single dominant value of k_x.

According to the distribution of the amplitudes of the Fourier components of the pulse (eq. [21]), most of the energy goes into the mode with $k_x \approx 0$. Thus, this mode is the one with the largest amplitude in the snapshots of the transversal velocity perturbation (Fig. 5, *bottom left*). The wavelength of the fast mode increases with height due to the rapid increase of the Alfvén velocity (see Figs. 2 and 3). As the wave comes to those heights where the sound speed is much lower than the Alfvén speed, its propagation speed becomes close to the local Alfvén speed (eq. [17]). Since the propagation speed becomes independent of the direction, the gradients of the Alfvén speed produce bending of the wave front due to refraction. The left part of the wave front of the fast mode (closer to the axis) propagates faster than its right part (farther from the axis). Finally, the wave reaches the height where its vertical wavenumber is equal to zero, and it reflects back to the photosphere. Note that the complete reflection does not occur at the $v_A = c_S$ level, but higher up in the atmosphere. The Wentzel-Kramers-Brillouin (WKB) solution considered below in § 6.3 confirms that this effect is due to the gradients of the Alfvén speed and not an artifact coming from the upper boundary conditions. The velocity variations of the fast mode are accompanied by magnetic field variations (Fig. 5, *top left*). After the reflection takes place, some variations of pressure also occur in the reflected wave (visible in Fig. 5, *top right*). The latter are due to its oblique propagation with respect to the magnetic field lines.

The same transformation is experienced by another fast mode, propagating to the left with respect to the vertical in the $v_A < c_S$ region. It is transformed into the fast mode in the $v_A > c_S$ region. This mode is visible as a weak perturbation in the transversal velocity snapshot at the left-hand side of the simulation domain. It is produced by the Fourier components of the pulse with negative k_x. It also propagates with the fast-mode speed and is accompanied by magnetic field variations. The pressure variations are absent in this mode. Since k_x is negative in this mode, its wave front is inclined to the left. The vertical gradients of the Alfvén speed make the right part of the wave front propagate faster than its left part, and thus it refracts toward the sunspot axis.

The second transformation observed at the $v_A = c_S$ line is a fast mode transformed into a slow (acoustic) mode in the $v_A > c_S$ region. According to § 3, the resulting slow-mode wave train is produced by the Fourier harmonics of the fast mode, whose directions of propagation stay within 5°–7° with respect to the longitudinal. The slow mode is visible in the longitudinal velocity snapshots. It propagates with a lower speed, close to the local speed of sound, and has a wavelength that is almost constant with height and is smaller than that of the fast mode. While the fast mode propagates across the magnetic field lines, the slow mode is channeled along them higher up to the chromosphere. The slow mode is generated with a rather low amplitude at the $v_A = c_S$ line, but its amplitude increases with height almost 3 times between $z = 350$ and 700 km, in accordance with the density falloff (the density scale height is $H_p \approx 130$ km at $z = 350$ km). The amplitude of the slow mode remains lower than that of the fast one everywhere in the $v_A > c_S$ region. Note that there are no variations in the magnetic field associated with the slow mode. Instead, it produces pressure variations with amplitude increasing with height, as expected for an acoustic wave.

The directions of the mode propagation can be explained by means of the arguments given in §§ 4 and 5. The slow mode is only present in the $v_A > c_S$ region. According to Figure 4, its direction of propagation (i.e., direction of energy propagation, given by $\boldsymbol{v}_g$) in this region should be close to the direction of the magnetic field lines, as is actually observed in the simulations. Consider now the fast mode with $k_x \approx 0$. The wavevector $\boldsymbol{k}$ is vertical for this mode. In the $v_A \approx c_S$ region, the group velocity vector of this mode deviates from the direction of $\boldsymbol{k}$ according to Figure 4. The angle that makes $\boldsymbol{v}_g$ with $\boldsymbol{k}$ has the opposite sign to the angle between $\boldsymbol{B}_0$ and $\boldsymbol{k}$. This means that $\boldsymbol{v}_g$, for this fast mode, is inclined to the left with respect to the vertical direction everywhere in our simulation domain. We calculated the direction of $\boldsymbol{v}_g$ from equation (19) for the local parameters of the atmosphere along the wave path and $k_x = 0$. This direction is plotted as a dashed line over the transversal velocity snapshots in Figure 6. It is clear that the fast mode in the numerical simulations follows this direction. In the particular case of the model atmosphere considered here, the direction of $\boldsymbol{v}_g$ almost coincides with the direction of $\nabla v_{\rm A}$. The latter is marked by a solid line, slightly inclined to the left, in Figures 5 and 6. It can be seen that, indeed, the $\nabla v_{\rm A}$ line separates the fast modes refracting to the right from those refracting to the left.

The good correspondence between the numerical simulations and the expectations from simple arguments given in §§ 4 and 5 leads to important conclusions. If we know the parameters of the magnetic structure (for example, if $v_{\rm A}$, c_S, and θ can be derived from observations), the direction of propagation of the fast and slow magnetoacoustic modes can be easily estimated from equations (16) and (19). The height where the reflection of the fast mode is produced is expected to lie somewhere in the region where $v_{\rm A}$ starts to be much larger than c_S. The direction of the refraction of the fast wave is defined by the $\nabla v_{\rm A}$ line.

6.2. *Horizontal Driving*

Figures 7 and 8 give the snapshots and temporal evolution for the simulation with a 10 s period and horizontal driving. In this simulation, most of the energy of the driver goes into the slow (magnetic) modes in the $v_{\rm A} < c_S$ region. The vertical wavelength of the perturbation is lower than in the previous case and is about 50 km, in agreement with Figure 3. Note that there is also a fast mode produced directly by the driver in the $v_{\rm A} < c_S$ region. This mode can be seen as a weak disturbance, with a larger wavelength propagating to the left with respect to the main wave train.

The transversal velocity in the $v_{\rm A} < c_S$ region is almost twice as large as the longitudinal velocity. The pressure perturbations are associated mainly with the longitudinal velocity perturbations. Since the latter have a rather small amplitude below the $v_{\rm A} = c_S$ level, the pressure perturbations are negligible there (Fig. 7, *top right*). Instead, the variations of the magnetic field (Fig. 7, *top left*) associated with the slow mode are relatively large, as expected for the magnetic mode propagating along the magnetic field lines. The transversal magnetic field variations caused by this mode are up to 30 G. The longitudinal magnetic field oscillations (not shown in the figure) are everywhere small in the domain and do not exceed 7 G.

After the mode transformation at the $v_{\rm A} \approx c_S$ region, three waves with different propagation directions can be distinguished in the $v_{\rm A} > c_S$ region. Most of the energy of the slow (magnetic) mode in the $v_{\rm A} < c_S$ region goes into the slow (acoustic) mode in the $v_{\rm A} > c_S$ region. The transformed slow wave again propagates along the magnetic field lines with increasing amplitude and is accompanied by pressure variations.

The second transformation is when the slow (magnetic) mode is transformed into the fast (magnetic) mode above the $v_{\rm A} = c_S$ line. This mode is evident in the transversal velocity variations (Fig. 7, *bottom left*). This conversion is possible in the linear case if the attack angle of $\boldsymbol{k}$ with respect to the magnetic field is small in the transformation region. Thus, the vector $\boldsymbol{k}$ of the fast mode after the transformation is inclined in the direction of $\boldsymbol{B}_0$, within a few degrees. This situation should be contrasted to the case of the vertical driving simulations, where the most energetic fast mode in the $v_{\rm A} > c_S$ region was produced by the fast mode with $\boldsymbol{k}$ directed along the vertical below. So, since the vertical gradients of the Alfvén speed are much stronger than its horizontal gradients, the fact that the wave train is initially inclined makes the refraction in the $v_{\rm A} \gg c_S$ region faster, and the wave is reflected at a lower height. The WKB solution, considered below in § 6.3, proves this idea. Since the amplitude of this fast mode is rather low, both longitudinal and transversal magnetic field variations almost disappear in the $v_{\rm A} > c_S$ region.

The third transformation observed in the simulations with the horizontal driver is when the fast (acoustic) mode coming from below is transformed into the fast (magnetic) mode. This mode produces a weak disturbance refracting to the left with respect to the $\nabla v_{\rm A}$ line, visible in the transversal velocity and magnetic field snapshots in Figure 7. This mode behavior is completely analogous to the one in the simulations with a vertical driver and was considered in the previous subsection.

The direction of propagation of the slow mode is that of the magnetic field lines everywhere in the simulation domain. It deviates slightly from this direction only when crossing the $v_{\rm A} = c_S$ line, since the inclination angle of $\boldsymbol{v}_g$ in this case is the largest (see Fig. 4). The direction of propagation of the fast modes, given by the value of $\boldsymbol{v}_g$ (Fig. 8, *dashed line*), and the reference line defining the direction of the wave refraction, $\nabla v_{\rm A}$, again describe rather well the behavior of the numerical solution.

An important conclusion is that, independent of a vertical or horizontal driving, we always generate a fast magnetic mode that refracts back to the photosphere and a slow acoustic mode that continues up to the chromosphere along the magnetic field lines. Despite the mode transformation, in both simulations, the longitudinal velocity variations preserve their phase below, at, and above the mixing $v_{\rm A} = c_S$ layer. Taking into account the small field inclination at the location of the driver (about 10°) in real observations of sunspots close to disk center, one would measure mainly the longitudinal component of the velocity variations. Thus, the velocity signals measured simultaneously at two heights, photospheric and chromospheric, should show a good correlation.

6.3. *WKB*

It is clear from the previous sections that the picture of mode transformation is rather complicated. We can use a WKB solution of the equations to gain extra understanding of the simulations. The WKB approach assumes that the wavelength of the perturbation is much smaller than the characteristic scale of the variations of the background atmospheric parameters. In the zeroth-order WKB approximation, we neglect the variation of the wave amplitude and consider only the variation of its phase; that is, we assume that all the variables in equations (1)–(4) depend on x, z, and time as $U = ae^{i\phi(x,z)}e^{-i\omega t}$ (where a is constant). To make the analytical solution easier, we neglect the force of gravity in equations (1)–(4) and assume that pressure, density, and temperature are constant. These simplifications are justified in the spirit of the WKB approximation, in which the inhomogeneity of the medium varies gradually relative to the wavelength of the perturbation. However, the magnetic field is allowed to vary in both the x and z directions. These assumptions imply the constancy of the sound speed, but the Alfvén speed can change. In the calculations described below, we have taken the variations of $v_{\rm A}$ to be as they are in the MHS model sunspot, irrespective of the reason that produces such variations.

After these simplifications, the following equation for the wave propagation can be obtained:

$$\frac{\partial^2 \boldsymbol{V}}{\partial t^2} = \frac{\gamma P_0}{\rho_0}\nabla(\nabla\cdot\boldsymbol{V}) + \{\nabla\times[\nabla\times(\boldsymbol{V}\times\boldsymbol{B}_0)]\}\times\frac{\boldsymbol{B}_0}{4\pi\rho_0}. \quad (22)$$

Substituting the WKB solution into this equation and neglecting all the second derivatives of $\phi(x,z)$, one gets a first-order nonlinear partial differential equation of the form

$$F(x, z, \phi, p, q) = \omega^4 - \omega^2\left(c_S^2 + v_A^2\right)\left(p^2 + q^2\right) + c_S^2\left(p^2 + q^2\right)\left(v_{Ax}p + v_{Az}q\right)^2 = 0, \quad (23)$$

where $p = \partial\phi/\partial x$, $q = \partial\phi/\partial z$, and F is a nonlinear PDE. The parameters p and q are equivalent to the horizontal and vertical wavenumbers, respectively. Equation (23) contains information about two magnetoacoustic modes, one fast and one slow. Applying a method of characteristics, one can transform this PDE into the following set of ordinary differential equations:

$$\frac{d\phi}{ds} = 2\omega^2,$$

$$\frac{dp}{ds} = -\frac{1}{2}\left(p^2 + q^2\right)\frac{\partial v_A^2}{\partial x} \pm \left[0.5\left(p^2 + q^2\right)^2\left(c_S^2 + v_A^2\right)\frac{\partial v_A^2}{\partial x} - 2c_S^2\left(p^2 + q^2\right)\left(v_{Ax}p + v_{Az}q\right)\left(\frac{\partial v_{Ax}}{\partial x}p - \frac{\partial v_{Az}}{\partial x}q\right)\right] \times\left[\sqrt{\left(p^2 + q^2\right)^2\left(c_S^2 + v_A^2\right)^2 - 4\left(p^2 + q^2\right)\left(v_{Ax}p + v_{Az}q\right)^2 c_S^2}\right]^{-1},$$

$$\frac{dq}{ds} = -\frac{1}{2}\left(p^2 + q^2\right)\frac{\partial v_A^2}{\partial z} \pm \left[0.5\left(p^2 + q^2\right)^2\left(c_S^2 + v_A^2\right)\frac{\partial v_A^2}{\partial z} - 2c_S^2\left(p^2 + q^2\right)\left(v_{Ax}p + v_{Az}q\right)\left(\frac{\partial v_{Ax}}{\partial z}p - \frac{\partial v_{Az}}{\partial z}q\right)\right] \times\left[\sqrt{\left(p^2 + q^2\right)^2\left(c_S^2 + v_A^2\right)^2 - 4\left(p^2 + q^2\right)\left(v_{Ax}p + v_{Az}q\right)^2 c_S^2}\right]^{-1},$$

$$\frac{dx}{ds} = p\left(c_S^2 + v_A^2\right) \mp \left[\left(p^2 + q^2\right)\left(c_S^2 + v_A^2\right)^2 p - 2pc_S^2\left(v_{Ax}p + v_{Az}q\right)^2 - 2c_S^2 v_{Ax}\left(p^2 + q^2\right)\left(v_{Ax}p + v_{Az}q\right)\right] \times\left[\sqrt{\left(p^2 + q^2\right)^2\left(c_S^2 + v_A^2\right)^2 - 4\left(p^2 + q^2\right)\left(v_{Ax}p + v_{Az}q\right)^2 c_S^2}\right]^{-1},$$

$$\frac{dz}{ds} = q\left(c_S^2 + v_A^2\right) \mp \left[\left(p^2 + q^2\right)\left(c_S^2 + v_A^2\right)^2 q - 2qc_S^2\left(v_{Ax}p + v_{Az}q\right)^2 - 2c_S^2 v_{Az}\left(p^2 + q^2\right)\left(v_{Ax}p + v_{Az}q\right)\right] \times\left[\sqrt{\left(p^2 + q^2\right)^2\left(c_S^2 + v_A^2\right)^2 - 4\left(p^2 + q^2\right)\left(v_{Ax}p + v_{Az}q\right)^2 c_S^2}\right]^{-1}. \quad (24)$$

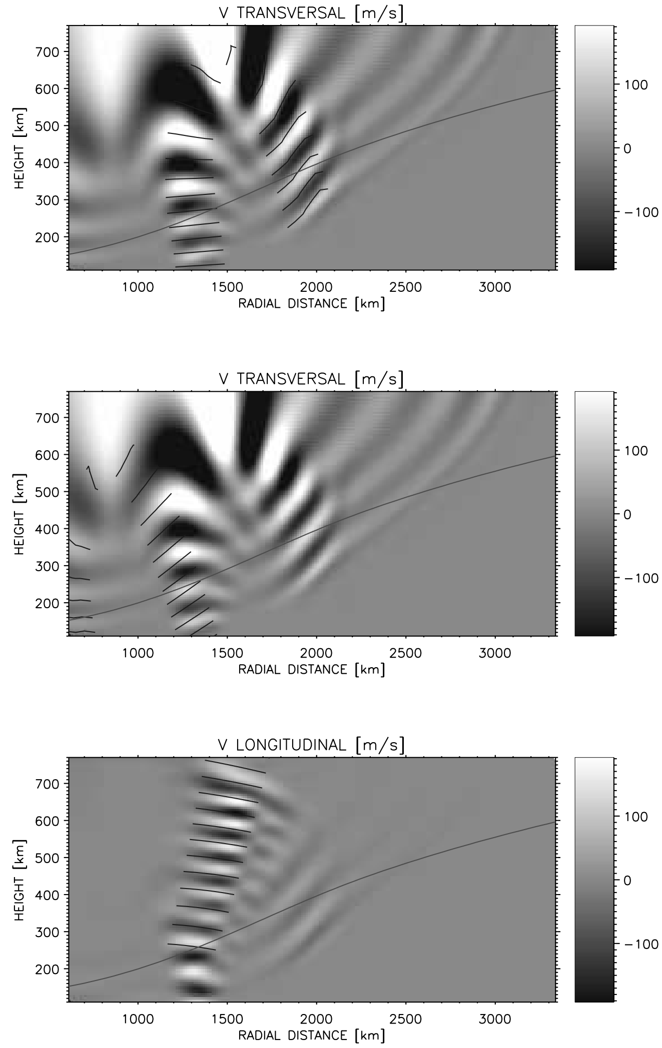

FIG. 9.—WKB solution for the simulations with a vertical driver. *Top*: Contours of constant phase of the WKB fast-mode solution, with $p = 0$, plotted over the transversal velocity from the numerical solution. *Middle*: Same as above, but using $p = -0.02$. *Bottom*: WKB slow-mode solution, with $p = 0$, plotted over the longitudinal velocity from the numerical solution. [*See the electronic edition of the Journal for a color version of this figure.*]

Here the variable s is the distance along the characteristic wave propagation path. The upper sign corresponds to the slow-mode solution, and the lower sign corresponds to the fast-mode solution (hereafter referred to as the "minus" and "plus" solutions, respectively). These five ODEs were solved numerically using a fourth-order Runge-Kutta method. As initial conditions, we took p equal to some value and calculated q from the dispersion relation, assuming constant v_A and c_S (solution of eq. [16]). The value of q is different for the plus and minus solutions, corresponding to the fast and slow waves. The sign of the WKB solution is maintained below and above the $v_A = c_S$ level; that is, a wave starting as a fast one continues to be fast, even after the ratio between the characteristic velocities changes. In the calculations described below, the values of c_S and v_A are taken from the MHS model atmosphere. The value of c_S is allowed to vary from point to point, despite the gradients of c_S being neglected in deriving equations (24). This influences the final solution very little, however. By varying x along the $z = 0$ axis, we can construct the particle paths with origins at different distances from the sunspot axis. The lines $z(x)$ give the directions of the group velocity of the solution. Similarly, ϕ gives us the phase of the

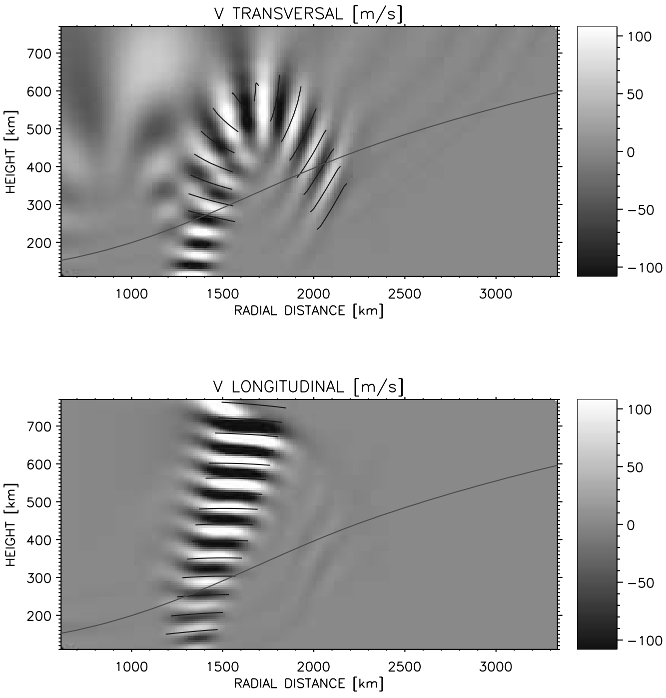

FIG. 10.—Same as Fig. 9, but for simulations with a horizontal driver. *Top*: WKB fast-mode solution, with $p = 0.01$. *Bottom*: WKB slow-mode solution, with $p = -0.01$. [*See the electronic edition of the Journal for a color version of this figure.*]

waves at different time moments (or, equivalently, different values of the parameter s). The contours of constant ϕ indicate the positions of the wave front. Note that the WKB solution takes into account the changes of the direction of the wave propagation due to both effects: wave refraction and inclination of $\boldsymbol{v}_g$ due to the anisotropy of the medium.

Figures 9 and 10 show the results of the WKB solution. The dark gray lines plotted over the simulated velocity fields are the contours of constant ϕ at a given time moment. In order to make the figures clear, only solutions with origins within the driver are taken. The phase difference between the adjacent wave fronts is kept constant within each snapshot and is 1.6 times larger for the transversal velocity snapshots than for the longitudinal ones. The constancy of the phase difference implies that the time difference between the wave fronts is constant as well.

Let us consider first the simulations with a vertical driver. The top panel of Figure 9 displays the WKB fast-wave solution with $p = 0$ (infinite horizontal wavelength). It confirms that the fast wave generated by the driver below the $v_{\rm A} = c_S$ line continues as a fast wave above this line. The phase speed of the fast wave increases with height. The right part of the wave front moves faster than its left part below the $v_{\rm A} = c_S$ level, and the opposite is observed above. At the top of the simulation domain, the vertical wavevector becomes equal to zero, and the wave refracts back to the photosphere. Note that the WKB solution describes rather well the inclination of the wave front and the propagation speed at every moment. The WKB approximation should break down when the wavelength of perturbation becomes comparable with the scale height of the atmosphere (see Table 1). This is the case even for the 10 s period simulations in which both H and λ are on the order of 100 km. If we take into account the simplifications of the "analytical" WKB solutions, the agreement between the simulations and this solution is surprising. As the only parameter allowed to vary is the Alfvén speed (the acoustic speed is assumed to be constant in the derivation of eq. [24]), we conclude that the main reason for the refraction of the fast mode is the gradient of $v_{\rm A}$ (Fig. 2).

The middle panel of Figure 9 gives another fast-wave WKB solution. In this case, the initial condition is $p = -0.02$ at the $z = 0$ level. The horizontal wavelength of such a wave is about 300 km, and the wave front is inclined initially to the left. As a result, this fast wave refracts toward the sunspot axis, and complete reflection occurs somewhat lower than in the case of the wave with $p = 0$. Note that the fast wave with nonzero k_x (or p) is already present in the $v_{\rm A} < c_S$ region and is generated by the driver due to its Gaussian shape in the x direction. Again, the numerical and the WKB solutions give very similar results.

The bottom panel of Figure 9 shows the slow-wave WKB solution with $p = 0$. In this case, the WKB can describe the longitudinal velocity only in the $v_{\rm A} > c_S$ region. Thus, it confirms that the slow wave is not present below the $v_{\rm A} = c_S$ level, but is generated after the mode transformation. The WKB solution describes correctly the path of this mode along the magnetic field lines. The propagation speed of the slow mode is almost constant with height.

The case of the simulations with a horizontal driver is presented in Figure 10. The bottom panel of this figure shows a slow WKB solution with $p = -0.01$ ($\lambda_x \sim 630$ km). The slow mode is generated at the photospheric level directly by the driver. The wave front of this mode is initially inclined, and the wave experiences a refraction, so it comes to the $v_{\rm A} = c_S$ line with a horizontal wavenumber different from the one at the lower boundary.

Finally, the top panel of Figure 10 gives the fast WKB solution with $p = 0.01$ ($\lambda_x \sim 630$ km). The fast-wave solution cannot describe the transversal velocity variations below the $v_{\rm A} = c_S$ line, so it confirms that this fast mode is generated after the mode transformation. As was pointed out in the previous section, this mode appears at the $v_{\rm A} = c_S$ line with a wave front that is inclined to the right (positive p). This makes the refraction easier, and the wave is reflected at a lower height than one with $p = 0$. Since the Alfvén speed is smaller at this height, it explains the lower wavelength of this fast mode.

From all these calculations, we conclude that the incidence angle of the fast mode on the $v_{\rm A} = c_S$ interface is unimportant for the reflection. The reference surfaces for the wave reflection are contours of constant $v_{\rm A}$ in the $v_{\rm A} \gg c_S$ region. However, since the gradients of c_S are often smaller than those of $v_{\rm A}$, the contours of constant $v_{\rm A}/c_S$ and constant $v_{\rm A}$ can be quite similar.

7. DISCUSSION

The simulations considered in this paper provide a nice demonstration of the complex behavior of the magnetoacoustic waves in a magnetic atmosphere with a realistic sunspot-like field geometry. They reveal that a periodic pulse located at the lower photosphere generates a set of fast and slow modes, each following a different path in the x-z plane and experiencing a different transformation at the $v_{\rm A} = c_S$ interface, depending on the initial inclination of the wave front. In all cases, the slow mode is guided along the magnetic field lines up to the chromosphere. In contrast, the fast mode suffers from refraction and complete reflection at heights where $v_{\rm A}$ is much larger than c_S. In the MHS model sunspot considered here, this height is located at the lower chromosphere. This behavior of the fast mode is independent of whether it is generated directly by the driver or if it appears after the mode transformation at the $v_{\rm A} = c_S$ line. It means that only some part of the energy of the driver is transported to the upper atmosphere. An important part of the energy is returned back to the photosphere by the fast mode. This makes the mechanism of energy transport by waves ineffective. It remains to be determined to what extent the amount of energy propagated upward may contribute to the heating of the high chromospheric layers.

The above conclusions are obtained on the basis of particular simulations of oscillations excited by a periodic driver localized in space at a certain distance from the sunspot axis. The period of the driver (10 s) was chosen in order to have a small wavelength of the waves, which allows us to see a clear picture of the wave transformations and refraction. Waves with frequencies above the acoustic cutoff should show a similar behavior, since the buoyant force does not play an important role. The difference between them should be quantitative, not qualitative, in nature. The conversion coefficients of modes at the $v_A \approx c_S$ region show a frequency dependence (Cally 2005, 2006; see § 3). The fast-to-slow mode transformation coefficient increases with decreasing frequency, and this transformation becomes possible even for waves propagating at large angles with respect to the magnetic field. At the same time, the fast-to-fast (and slow-to-slow) mode transformation coefficient decreases with decreasing frequency. If we apply these reasonings to our simulations, this would lead to a redistribution of the energy that goes into a fast or slow mode at the $v_A > c_S$ region after the transformation, depending on the type of excitation (horizontal or vertical). Namely, the large-period waves excited by a vertical pulse would show a tendency to remain acoustic through the whole atmosphere (fast waves below $v_A = c_S$ and slow waves above) and would transport the energy of the pulse to the upper layers. In the case of a horizontal excitation, most of the energy after the transformation would go into the magnetic mode and thus would return to the photosphere. This is different from the 10 s period simulations, where the energy that goes into the fast or slow modes after the transformations is of the same order of magnitude, independent of the excitation. It means that the part of the energy that is transported to the upper layers depends closely on the excitation mechanism that produces oscillations in sunspots.

The relatively small size of our MHS model sunspot does not allow us to study waves with more realistic periods numerically. Due to their large spatial wavelengths, waves with 3–5 minute periods do not fit into the simulation domain. However, in order to extend our results to the case of waves with more realistic periods, we present in Figure 11 an example of a simulation with a horizontal driver of 50 s periodicity. The figure gives snapshots of the transversal and longitudinal velocity components, together with the corresponding WKB solution (see § 2.4 for details). The snapshots are taken at the moment when the reflected fast wave has returned to the bottom border of the simulation domain. It follows from Figure 11 that the qualitative picture of this simulation is similar to that with the 10 s period (compare to Fig. 10). The slow mode is excited by the driver and propagates as a slow mode through the transformation region. The fast mode is produced after the transformation by a Fourier component of the pulse with a nonzero horizontal wavelength. Due to the larger spatial period of 50 s oscillations, it is more difficult to get a clear picture of the mode transformations, but the comparison with the 10 s case is very helpful. Both the fast and slow WKB solutions plotted over the simulations are completely analogous to those in the 10 s case (see Fig. 10) with the parameter p (horizontal wavelength) that is 5 times smaller, indicating a 5 times larger wavelength of oscillations, as expected for a temporal period that is 5 times larger. However, the fit of the WKB solution to the numerical solution is not as good as in the 10 s case. The fast-mode refraction is somewhat slower in the numerical solution. This is not surprising, since the wavelength in the 50 s case is larger than the characteristic scale of the density falloff, and the approximations leading to the WKB solution are not valid.

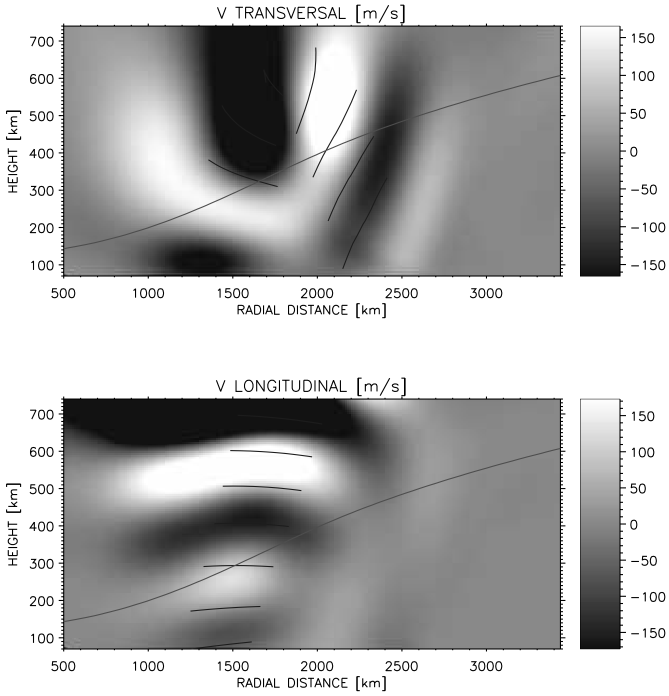

Fig. 11.—Snapshots of transversal (*top*) and longitudinal (*bottom*) velocity at the elapsed time 150 s after the start of the simulations, with a horizontal driver of 50 s period, together with the WKB solution. *Top*: WKB fast-mode solution, with $p = 0.002$. *Bottom*: WKB slow-mode solution, with $p = -0.002$. [*See the electronic edition of the Journal for a color version of this figure*.]

Figure 12 presents another simulation that helps to generalize our conclusions. In this simulation, the initial condition consists of an instantaneous pressure pulse located at the lower boundary (see eq. [14]). The pulse has a Gaussian shape in the x and z directions and thus gives rise to a set of fast and slow modes with different values of k_x and k_z. The latter implies different temporal periods of such waves on a rather wide range. The temporal evolution of this pulse, composed of waves with different periods, is shown in Figure 12. Similar to the case of the periodic driver, longitudinal and transversal velocity components are plotted to make the fast and slow magnetoacoustic modes distinct. The inspection of this figure leads to the following conclusions. The slow modes generated by the pulse are directed along the magnetic field lines, and their propagation speed is that of a local speed of sound (Fig. 12, *right*). They move upward from the photosphere to the chromosphere through the transformation region with very little dispersion. This means that all slow waves, with different periods, follow closely the same behavior. The temporal evolution of the fast-wave part of the pulse is given in the left panels of Figure 12. The propagation speed in this case is much larger. The fast-wave pulse shows a symmetry with respect to the ∇v_A line. At a certain height in the $v_A \gg c_S$ region, the pulse splits into two components, one refracting to the left with respect to the ∇v_A line and another one refracting to the right. A complete reflection of the fast waves is produced higher in the atmosphere. Again, very little dispersion is observed. It suggests that all fast waves with different periods follow a similar behavior. Thus, this simulation strengthens the conclusion that waves in sunspots cannot be considered as an efficient mechanism for energy transport to the upper atmosphere. Since waves in a rather wide range of periods behave

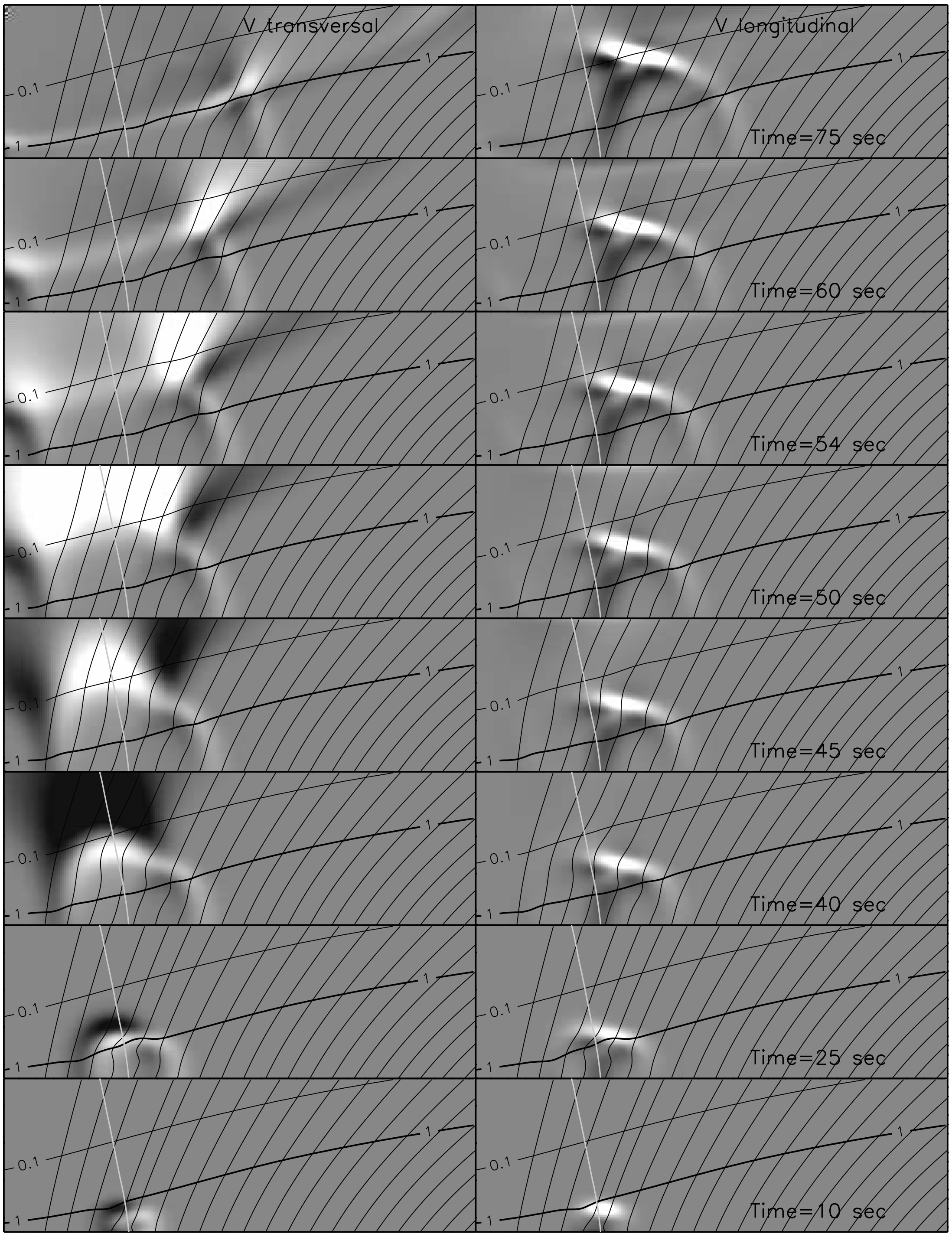

Fig. 12.—Time evolution of the longitudinal and transversal velocity components in simulations with an instantaneous pressure pulse as the initial condition. Note that the snapshots are not equidistant in time.

similarly, it suggests that only a part of the energy of the driver is transported to the chromosphere by the slow mode, while the energy contained in the magnetic fast mode is returned back to the photosphere.

These conclusions can be generalized further. Figure 13 gives wave paths, obtained from the WKB solution, for the fast and slow modes generated at different distances from the sunspot axis in our model atmosphere (p is assumed to be equal to 0 in all cases, and the period of the waves is 10 s). It shows that the waves behave similarly to the case of the numerical solution considered in the paper. In particular, the direction of propagation of the slow mode is that of magnetic field lines in the $v_A > c_S$ region. Below, in the $v_A < c_S$ region, it deviates slightly from this direction, mainly because the gradients of v_A modify the wave propagation path. The fast mode $\boldsymbol{v}_g$ has a direction close to the ∇v_A line, unless v_A is significantly larger than c_S. Once the fast mode reaches the heights where $v_A \gg c_S$, the refraction and complete reflection is produced in all the cases. The reflection height of the fast mode changes with distance from the sunspot axis. In our rather realistic model sunspot, this height increases

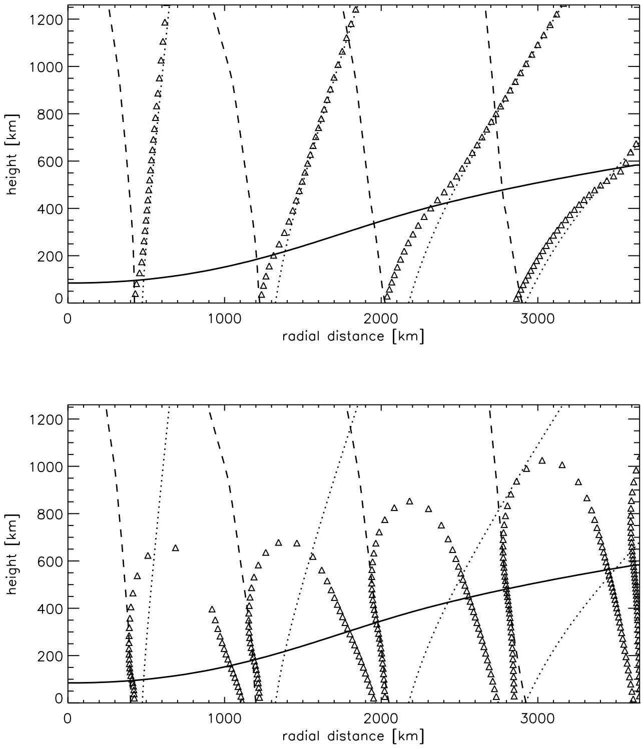

FIG. 13.—Wave paths (*triangles*) of the slow (*top*) and fast (*bottom*) modes calculated in the WKB approximation. Dotted lines represent the magnetic field lines, dashed lines represent the $\nabla v_{\rm A}$ lines, and the solid line represents $v_{\rm A} = c_S$.

from 600 to 1000 km as r changes from 0 to 4000 km. Above this height only the slow mode exists. Thus, the energy contained in the fast mode reaches at most the base of the chromosphere, and most of it is reflected in the temperature minimum region. Since oscillations of the magnetic field are associated primarily with the fast mode, it is expected that no significant oscillations can be observed above the temperature minimum height in the sunspot umbra. The fraction of the energy of the driver that goes into the fast or slow mode depends on its distance to the axis (i.e., inclination of the magnetic field lines), its height in the atmosphere, and the spectrum of $\boldsymbol{k}$ that it produces. It is of interest to perform simulations to determine this fraction as a function of the size of the magnetic structure and its field configuration.

8. CONCLUSIONS

In this paper we have considered linear oscillations in a rather realistic sunspot-like magnetic field structure. The oscillations are excited by a periodic driver localized in space with a period of 10 s. In addition, the temporal evolution of an instantaneous pressure pulse has been inspected. Different processes that affect the direction of wave propagation and mode transformation are discussed separately, based on a simple model of magnetoacoustic modes in a homogeneous atmosphere. We find that simple qualitative arguments concerning the direction of the mode propagation in an anisotropic medium and wave refraction agree rather well with results from numerical simulations. This gives additional proofs of the results of the numerical solution.

Getting all these ingredients together allows us to make some important conclusions:

1. Since in an anisotropic medium the directions of the phase and group velocities do not generally coincide, the fast and slow modes generated by the same driver always propagate in different directions in the *x-z* plane, understanding as the direction of propagation that of $\boldsymbol{v}_g$.
2. Given a magnetic structure, the directions of $\boldsymbol{v}_g$ for the fast and slow modes can be estimated if we know the values of c_S, $v_{\rm A}$, and ψ. The *slow* mode is always guided along the magnetic field lines, except at the region in which $v_{\rm A} \approx c_S$, where it deviates in a direction that depends on the value of the angle between $\boldsymbol{B}_0$ and $\boldsymbol{k}$. The *fast*-mode direction of propagation is that of $\boldsymbol{k}$, independent of the magnetic field inclination. The exception is in the region in which $v_{\rm A} \approx c_S$, where it makes an angle with $\boldsymbol{k}$, depending on the inclination of $\boldsymbol{B}_0$ with respect to $\boldsymbol{k}$ (eq. [19]).
3. The fast mode experiences refraction due to the gradients of $v_{\rm A}$. The height for complete reflection is expected to lie high in the atmosphere in a region where $v_{\rm A}$ starts to be much larger than c_S. In the model sunspot considered in this paper, this height is located at about 600–1000 km; that is, at the base of the chromosphere. If horizontal gradients of $v_{\rm A}$ are present, waves refracting to the left are separated from waves refracting to the right by the $\nabla v_{\rm A}$ line. The height for complete reflection depends on the angle between $\nabla v_{\rm A}$ and $\boldsymbol{k}$.
4. A periodic driver located in the region in which $v_{\rm A} < c_S$ gives rise to fast and slow magnetoacoustic modes. The particular set of modes that are generated depends on the horizontal shape of the driver (taken to be a Gaussian profile in the simulations considered here). Each Fourier component of the pulse experiences a different transformation at the $v_{\rm A} = c_S$ line, according to its particular value of k_x.
5. After the mode conversion at the $v_{\rm A} = c_S$ layer, the fast mode is reflected back to the photosphere, while the slow mode is guided along the magnetic field lines up to the chromosphere. This behavior is similar for waves with different periods generated at different distances from the sunspot axis. Thus, only some part of the energy of the pulse is transported to the upper atmosphere. An important part of the energy is returned back to the photosphere by the fast mode. This makes the mechanism of energy transport by waves ineffective.

We are grateful to A. Hood for the idea of the WKB solution and to the Solar and Magnetospheric MHD Theory Group at the University of St. Andrews for discussions. This work was partially supported by the Spanish Ministerio de Educación y Ciencia through project AYA2004-05792.

REFERENCES

Avrett, E. H. 1981, in The Physics of Sunspots, ed. L. E. Cram & J. H. Thomas (Sunspot: Sacramento Peak Obs.), 235
Bellot Rubio, L. R., Collados, M., Ruiz Cobo, B., & Rodríguez Hidalgo, I. 2000, ApJ, 534, 989
Berenger, J.-P. 1994, J. Comput. Phys., 114, 185
———. 1996, J. Comput. Phys., 127, 363
Bogdan, T. J. 2000, Sol. Phys., 192, 373
Bogdan, T. J., & Judge, P. G. 2006, Philos. Trans. R. Soc. London A, 364, 313
Bogdan, T. J., & Knölker, M. 1989, ApJ, 339, 579
Bogdan, T. J., et al. 2002, Astron. Nachr., 323, 196
———. 2003, ApJ, 599, 626
Cally, P. S. 2001, ApJ, 548, 473
———. 2005, MNRAS, 358, 353
———. 2006, Philos. Trans. R. Soc. London A, 364, 333
Cally, P. S., & Bogdan, T. J. 1993, ApJ, 402, 721
———. 1997, ApJ, 486, L67
Cally, P. S., Bogdan, T. J., & Zweibel, E. G. 1994, ApJ, 437, 505
Cargill, P. J., Spicer, D. S., & Zalesak, T. 1997, ApJ, 488, 854

Cattaneo, F., Emonet, T., & Weiss, N. 2003, ApJ, 588, 1183
Centeno, R., Collados, M., & Trujillo Bueno, J. 2006, ApJ, 640, 1153
Hasan, S. S., Kalkofen, W., van Ballegooijen, A. A., & Ulmschneider, P. 2003, ApJ, 585, 1138
Hasan, S. S., & Ulmschneider, P. 2004, A&A, 422, 1085
Hasan, S. S., van Ballegooijen, A. A., Kalkofen, W., & Steiner, O. 2005, ApJ, 631, 1270
Hirsch, C. 1990, Numerical Computation of Internal and External Flows (Chichester: Wiley)
Hu, F. Q. 1996, J. Comput. Phys., 129, 201
Hu, F. Q. 2001, J. Comput. Phys., 173, 455
Landau, L. D., & Lifshitz, E. M. 1984, Electrodynamics of Continuous Media (Oxford: Pergamon)
Marsh, M. S., & Walsh, R. W. 2005, in Proc. International Scientific Conf. on Chromospheric and Coronal Magnetic Fields, ed. D. E. Innes, A. Lagg, & S. K. Solanki (ESA SP-596; Noordwijk: ESA), 75
Osterbrock, D. E. 1961, ApJ, 134, 347
Parchevsky, K. V., & Kosovichev, A. G. 2005, AGU Fall Meeting 2005, Abstract SH41A-1118
Pizzo, V. J. 1986, ApJ, 302, 785
Qi, Q., & Geers, T. L. 1998, J. Comput. Phys., 139, 166
Rosenthal, C. S., & Julien, K. A. 2000, ApJ, 532, 1230
Rosenthal, C. S., et al. 2002, ApJ, 564, 508
Spruit, H. C. 1974, Sol. Phys., 34, 277
———. 1981, A&A, 102, 129
Staude, J. 1999, in ASP Conf Ser. 184, Third Advances in Solar Physics Euroconference: Magnetic Fields and Oscillations, ed. B. Schmieder, A. Hofmann, & J. Staude (San Francisco: ASP), 113
Vernazza, J. E., Avrett, E. H., & Loeser, R. 1981, ApJS, 45, 635
Vögler, A., Shelyag, S., Schüssler, M., Cattaneo, F., Emonet, T., & Linde, T. 2005, A&A, 429, 335
Weiss, N., Brownjohn, D. P., Hurlburt, N. E., & Proctor, M. R. E. 1990, MNRAS, 245, 434
Zhugzhda, Y. D., & Dzhalilov, N. S. 1982, A&A, 112, 16
———. 1984, A&A, 132, 52